Compendium of M.Sc. Publications on Numerical Estimation of Effective Properties of Porous Materials

Maria Camila Osorno Tejada

UNIVERSIDAD EAFIT
COLLEGE OF ENGINEERING
MASTER PROGRAM IN ENGINEERING
MEDELLIN, COLOMBIA
MAY 2014

MASTER PUBLICATION

Compendium of M.Sc. Publications on Numerical Estimation of Effective Properties of Porous Materials

MASTER STUDENT

Maria Camila Osorno Tejada

ADVISORS

Prof. Dr. Eng. Oscar Ruiz
CAD CAM CAE Laboratory, Universidad EAFIT

Prof. Dr. Eng. Holger Steeb
Institute of Mechanics-Continuum Mechanics,
Ruhr-University Bochum

Submitted in partial fulfillment of the requirements for the degree of Master of Engineering in the College of Engineering of the EAFIT University

UNIVERSIDAD EAFIT
COLLEGE OF ENGINEERING
MASTER PROGRAM IN ENGINEERING
MEDELLIN, COLOMBIA
MAY 2014

Contents

List of Figures

List of Tables

Acknowledgements

I want to thank my family, without their love and support this would have never been possible.

I want to express my gratitude to my advisor Prof. Dr. Eng. Oscar Ruiz for his guidance and invaluable recommendations. Also, I want to thank Prof. Dr. Eng. Holger Steeb for his support during my stay at the Chair of Continuum Mechanics at Ruhr Universität Bochum.

Many thanks to David Uribe for his accompaniment and help. I want to thank to the assistants and friends at the Laboratory of CAD CAM CAE for their companionship, specially Jorge Correa, Mauricio Aristizabal, Camilo Cortes, Santiago Arroyave, Mateo Alzate, Daniel Burgos, Felipe Escobar and Sebastian Sarmiento.

My grateful acknowledgements to the Laboratory of CAD CAM CAE at Universidad EAFIT, the Institute of Mechanics at Ruhr-Universität Bochum and the Colombian Administrative Department of Sciences, Technology and Innovation (COLCIENCIAS) for the financial and technical support for the presented research and my master studies.

Introduction

The characterization of mechanical and transport phenomena of porous media is of high relevance in bio-mechanics, geophysics, manufacturing, environmental sciences, among other fields. Properties that are of interest to this fields are porosity, permeability, tortuosity and compressional and shear moduli.

Laboratory and field experiments that estimate this properties present numerous technical difficulties, high expenses and require long periods of time. In contrast, numerical estimation of effective properties of porous materials presents advantages such as that only one material sample is needed to calculate several properties and the process takes relatively short time. The numerical estimation of material properties requires previous knowledge of the porous medium's geometry. There are different methods to acquire the sample geometry, such as micro computer tomography, positron emission tomography, magnetic resonance imaging and the generation of artificial geometries.

Micro-CT is becoming more accessible, and presents the advantage of representing faithfully the internal structure of the analysed material. The main disadvantage of estimation of effective properties from micro-CT geometry data is the need of domains large enough to be representative of the porous medium's microstructure. This translates into file sizes in the range of tens of kilobytes. This large quantity of data presents difficulties on its manipulation. It is necessary to develop methodologies that allow the modelling of physical phenomena in large domains, by applying techniques such as the parallelization of computational algorithms.

This work consists on the compilation of the research performed at the Laboratory of CAD CAM CAE at Universidad EAFIT and the Institute of Mechanics at Ruhr-Universität Bochum. The results presented involve a combination of Computational Geometry and Computational Mechanics. Table 0.1 presents a summary of the papers presented in the thesis.

Producto	Referencia
Accepted article in international conference.	Uribe, D., Osorno, M., Steeb, H., Saenger, E. H. & Ruiz O. (2014). Geometrical and numerical modeling for porous media wave propagation. Proceedings of TMCE. Budapest, Hungary.
Published article international journal	Osorno, M., Steeb, H., Uribe, D., & Ruiz, O. (2013). Estimation of large domain Al foam permeability by Finite Difference methods. PAMM, 13(1), 247-248. ISSN 1617-7061.
Article pending submission in international journal.	Osorno, M., Steeb, H., Uribe, D., & Ruiz, O. (2013). Finite Difference Estimation of Permeability in Large Domains in a Wide Porosity Range.
Accepted article in international conference.	Osorno, M., Uribe, D., Saenger, E. H., Madonna, C., Steeb, H. & Ruiz O. (2014). Numerical estimation of carbonate properties using a digital rock physics workflow. Proceedings of EAGE. Amsterdam, Netherlands.
Article presented in international conference.	Uribe, D., Osorno, M., Sivanesapillai, R., Steeb, H. & Ruiz O. (2014). 85^{th} Annual Meeting of the International Association of Applied Mathematics and Mechanics (GAMM) in Erlangen, Germany.

TABLE 0.1. Presented articles

The research presented here was funded in collaboration between the Laboratory of CAD CAM CAE at Universidad EAFIT, the Institute of Mechanics at Ruhr-Universität Bochum and the Colombian Administrative Department of Sciences, Technology and Innovation (COLCIENCIAS).

Chapter 1 proposes a generic workflow for modelling the geometry of porous materials from CT-scans. The geometrical representation obtained is tested with a numerical simulation of physical phenomena against laboratory experiments.

In chapter 2 the permeability of an aluminum foam sample is estimated by simulating a Stokes flow through the material using the Finite Difference method. In chapter 3 this approach is benchmarked with different porous materials in a wide range of porosities and a parallel solver is implemented to simulate the Stokes flow through large domains that are representative of the material micro-structure.

Chapter 4 proposes a workflow to characterize Hauptmuschelkalk (carbonate characterized by its low porosity), implementing a image segmentation procedure and calculating the carbonate permeability and the effective wave velocity as a function of the estimated porosity.

Chapter 5 presents a geometrical method to estimate the hydraulic tortuosity limits with respect to Reynolds numbers of a fibrous porous medium. The method presents an advantage by excluding the calculation of high Reynolds flow simulations, which often present computational difficulties.

Finally, chapter 6 summarizes the observations of the reviewers in the writing, submission and publication processes of the papers, and the response given to each observation.

CHAPTER 1

Geometrical and numerical modeling for porous media wave propagation

D. Uribe[1,2], M. Osorno[1,2], H. Steeb[2], E.H. Saenger[3] and O. Ruiz[1]
[1] CAD/CAM/CAE Laboratory, Universidad EAFIT, Medellin, Colombia.
[2] Institute of Mechanics, Ruhr-University Bochum, Germany.
[3] Geological Institute, ETH Zürich, Switzerland.

This paper presents a workflow for geometrically modelling porous materials from micro CT scan data going through different geometrical representations. The proposed workflow is applied to an aluminum foam CT scanned sample, and the resulting geometrical model is tested with a numerical simulation of wave propagation. The different geometrical representations allow the use of commercial CAE software and facilitate the collaboration between different research groups.
This work was made on collaboration between the Laboratory of CAD CAM CAE at Universidad EAFIT, the Institute of Mechanics at Ruhr-University Bochum and the Geological Intitute at ETH Zürich. This paper was accepted on the Conference TMCE. Budapest, Hungary. May, 2014.

Abstract. Determining hydro-mechanical properties of porous materials present a challenge because they exhibit a more complex behaviour than their continuous counterparts. The geometrical factors such as pore shape, length scale and occupancy play a definite role in the materials characterization. On the other hand, computational mechanics calculations for porous materials face an intractable amount of data. To overcome these difficulties, this investigation propose a workflow (Image segmentation, surface triangulation and parametric surface fitting) to model porous materials (starting from a high-resolution industrial micro-CT scan) and transits across different geometrical data (voxel data, cross cut contours, triangular shells and parametric quadrangular patches) for the different stages in the computational mechanics simulations. We successfully apply the proposed workflow in aluminum foam. The various data formats allow the calculation of the tortuosity value of the material by using viscoelastic wave propagation simulations and poroelastic investigations. Future work includes applications for the geometrical model such as boundary elements and iso-geometrical analysis, for the calculation of material properties.

Keywords

Computational mechanics, geometric modeling, porous materials, wave propagation.

Nomenclature

$G = (\mathbf{P}, E)$	=	Graph with vertex set $\mathbf{P}$ and edge set E, nearly embedded in S_0
P	=	Pressure scalar field of a fluid occupying Ω. $P : \Omega \to \mathbb{R}$.
S_0	=	2-manifold (possibly disconnected, with border) surface corresponding to the isosurface $V(p) = V_{TR}$ for $p \in \Omega$.
T	=	$\{t_1, t_2, \ldots\}$ triangular mesh of triangles t_i with vertices in $\mathbf{P}$
V	=	A scalar field $V : \Omega \to \mathbb{R}$ produced by the CT scan of Aluminum Foam in Ω.
V_{TR}	=	Threshold real value in Hounsfield units which marks the presence of Aluminum Foam in a CT scan.
Ω	=	Rectangular prism aligned with the world axes such that $\Omega \subset \mathbb{R}^3$.

1. Introduction

Micro-scale Computational Mechanics studies of porous media are limited by the difficulty in geometrically modelling the microstructure material in an accurate

manner. The cavities are extremely small, the data size is very significant, and the data is present in unusable formats, since (e.g.) Voxel-based geometries cannot be used in most commercial structural mechanics and computational fluid dynamics software.

Researchers take two approaches: (i) Create their own geometries, based on abstraction of the subscale geometries. Examples are the so called 'packed spheres', lattices from convex uniform honeycombs, boolean operations with spheres or ellipsoids, Gaussian random fields, among others ([1], [2]). (ii) Use actual scan samples of porous media geometries that are based on CT scan data, which favors the usage of regular grid numerical methods. These methods have shortcomings in imposing boundary conditions, dealing with high frequency saw-tooth geometries, and describing curved boundaries with large numbers of degrees of freedom.

In this article we implement and apply several geometrical processing methods to represent solids from industrial micro CT scans of porous materials. The different representations of the material (voxels, contours, triangular meshes and parametric surfaces), allow simulations in the middle steps of the process. We can also manage the information about the porous media geometry with a lower memory usage. Finally with the parametric surfaces of the material, is possible the use of robust commercial CAE software that can not manage voxel-based information.

The workflow of our method begins by processing the micro-CT scan data using image segmentation algorithms (multiple thresholding, watershed algorithms). The segmented data represents enumerations, 3D scalar fields and planar cross sections, which are used to build 3D shell and solid information by using several algorithms: Marching Cubes, Poisson, 2-D similarity Voronoi- Delaunay generalized lofting, Power Crust and Surface Optimization. Parallelized computations have been applied, using as a unit cubic sub-domains of the general domain.

We have successfully created the enumeration, cross sectional, triangular and parametric representation of aluminum foam. From those representations, it was possible to estimate geometric properties, such as: porosity, lattice cross sectional area and shapes, and pore radius. The geometric properties were used on analytical solutions of wave propagation in porous media and compared with independent numerical simulations. The tortuosity is estimated, using the Geometrical Scenario formed, in two manners: Using Biot's poroelastic approach (a) The flow velocity is calculated and from it, the tortuosity. (b) Virtually stiffening the aluminium foam, calculating the flow velocity and from it the tortuosity. The results closely match each other.

This paper is organized as follows: Section 2 reviews the literature existent on the geometrical modeling of materials with micro-structure. Section **??** explains the various geometrical methods aligned to model the porous materials. Section **??** discusses computational mechanics methods mounted on the geometrical models, presenting the achieved results on mechanical properties and performance. Section 5 concludes the article and enumerates open research areas.

2. Literature Review

The reconstruction of surface and solid from CT-data is a common problem in computational geometry and visualization, but authors usually only focus in a specific part of the workflow: 1) Image segmentation, 2) Surface triangulation, 3) Parametric surface fitting.

Wirjardi ([3]) exposes a survey on the more common techniques for image segmentation, such as thresholding ([4], [5]), region growing ([6]) and deformable surfaces ([7]). Usually additional techniques are applied to correct noise and other data adquisition defects. Iassonov, et al. ([8]) proposes Image Analysis Normalization for image correction.

Several authors have proposed methods for surface triangulation from image segmented data. Lorensen et al. ([9]) propose an algorithm (Marching cubes) that generate a triangulation from voxels data employing a table of edge intersections. Amenta et al. ([10]) propose the Power crust algorithm which generates a triangulated mesh form a point set data. The obtained result does not depend on the data quality, but has the disvantage that only works with surface points. Ruiz et al. ([11]) recover a triangulated surface from slice samples by using 2D shape similarity. This method can be used when a topological faithfulness is really needed, but implies pre-processing to obtain 2D slices from the CT-scan data.

Different methods have also been proposed for generate parametric surfaces from points clouds or meshes. Kazhdan et al. ([12]) solve the problem of generating surfaces form a point data set treating it like the solution of Poisson equation. A good detail level is possible but the input data set must have ordered points. Ruiz et al. ([13]) present a stochastic approach to surface reconstruction from noisy points data set based on Principal Component Analysis, which has a good behaviour with non self-intersecting curves. Other proposed methods for generating parametric surfaces can be seen in [14], [15] and [16].

The reviewed methods present some disadvantages as restriction in the input data and high computational requirements. In this paper we propose a workflow for applying more efficient methods to obtain a geometrical model that can be used suitably for numerical simulation of effective material properties.

3. Methodology

Consider a domain $\Omega \subset \mathbb{R}^3$ forming a rectangular prism aligned with the axes of $\mathbb{R}^3$. The domain Ω contains a porous material. A computer tomogram of Ω results in a scalar field $V : \Omega \to \mathbb{R}$ which corresponds to the absorption of the X-rays by the material, measured in Hounsfield units. The CT scanner used has a resolution of 60 micrometers / Voxel.

In the present case the analysed porous material is 10 ppi AlSi7Mg foam (Fig. 1.1) by m.pore GmbH. Tab. 1.1 shows the modelling parameters of the aluminum

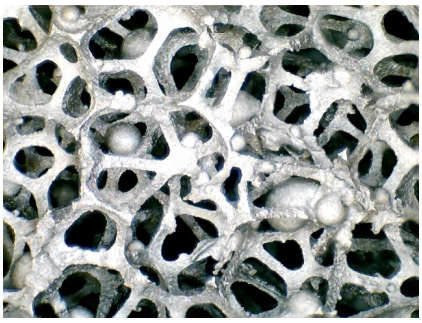

FIGURE 1.1. Aluminum Foam micro-structure.

foam.

The goal of this section is to describe the different algorithms used in this investigation to obtain explicit representations of S_{TR}., suitable for numerical calculations of effective hydro-mechanical properties.

3.1. Iso-Surface Occupancy.

- **Given:**
  (1) A scalar field $V : \Omega \to \mathbb{R}$.
  (2) A real (threshold) value V_{TR} in the range of V.
- **Goal:**
  (1) T triangulation approximating $V(p) = V_{TR}$ for $p \in \Omega$.

This part of the process is conducted by using a variation of the Marching Cubes algorithm ([9]). The triangulation T must have the characteristics of 2-manifoldness. Notice that $T \approx S_0$ has borders and it is possibly disconnected within Ω.

3.2. Cross-section-based Surface Reconstruction.

3.2.1. *Iso-Curve Occupancy.*

- **Given:**
  (1) A slice k-th of the CT scan in plane Π_k with normal Z.
  (2) A real (threshold) value V_{TR} in the range of V.
- **Goal:**
  (1) A set $\partial V \cup_k = \{\Gamma_0, \Gamma_1, ...\}$ of closed contours Γ_j , $j = 0, 1, ...$ on Π_k, which compose the boundary $\partial V \cup_k$ of the set $V \cup_k = \{p \in \Pi_k | V(p) \geq V_{TR}\}$.

Fig. 2(a) shows a typical slice Π_k of the CT scan. Each pixel (i, j) of the Π_k slice corresponds to the point $(x_i, y_j, z_k) \in \Omega \subset \mathbb{R}^3$. Fig. 2(a) displays the pixels with $V(x_i, y_j, z_k) \geq V_{TR}$. Each pixel represents a diminute square inside Π_k., and the 2D boolean union of pixels inside the foam results in a 2D region with city-block jagged boundary $\partial V \cup$ in Fig.2(b). A smoothing of these jagged contours using a Catmull-Rom interpolation produces the smooth contours in Fig. 2(c). Since the foam may have internal disconnected cavities, the cross sections $V \cup$ of the foam present holes, and their boundary ∂VU has several disconnected components ($\partial V \cup = \{\Gamma_0, \Gamma_1\}$). In our discussion, Γ_0 represents an external foam

contour and Γ_i for $i = 1, 2, ...$ represent the internal contours. The collection of such cross sections for a particular neighborhood of Ω is shown in Fig. 3(a).

If the distance between scan planes is considered, volumetric pixels (Voxels) are formed, which correspond to the parts of Ω filled by the aluminum foam (Fig. 3(b)).

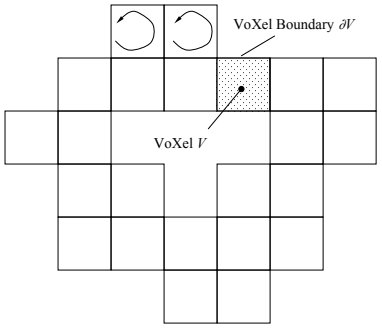

(a) Set of Voxels with 6000 above threshold.

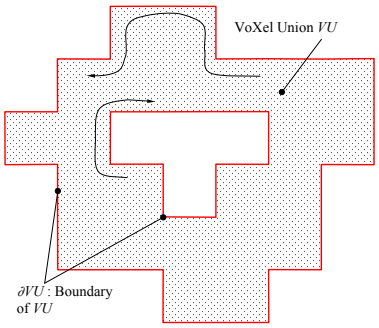

(b) Boolean Union of Voxels. City Block Contours.

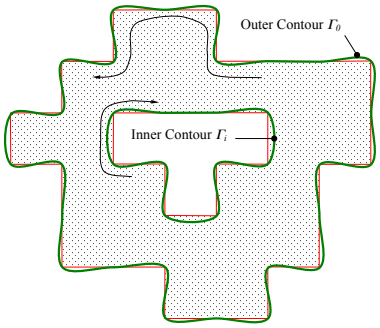

(c) Catmull-Rom smoothing of City Block Contours.

FIGURE 1.2. Contour Construction from CT Voxel per-slice Data.

3.2.2. *2D-similarity-driven Voronoi-Delaunay Algorithm.*

- **Given:**
  (1) A sequence of parallel cross sections of the domain Ω, Π_k with $k = 1, 2, ...$
  (2) A set $\partial V \cup_k = \{\Gamma_0, \Gamma_1, ...\}$ of closed contours Γ_j , $j = 0, 1, ...$ on Π_k, which compose the boundary $\partial V \cup_k$ of the set $V \cup_k = \{p \in \Pi_k | V(p) \geq V_{TR}\}$.
- **Goal:**
  (1) A sequence of triangular mesh surfaces $T_{i,i+1}$ that map the contours $\partial V \cup_i$ of level Π_i, onto the contours $\partial V \cup_{i+1}$ of level Π_{i+1}.

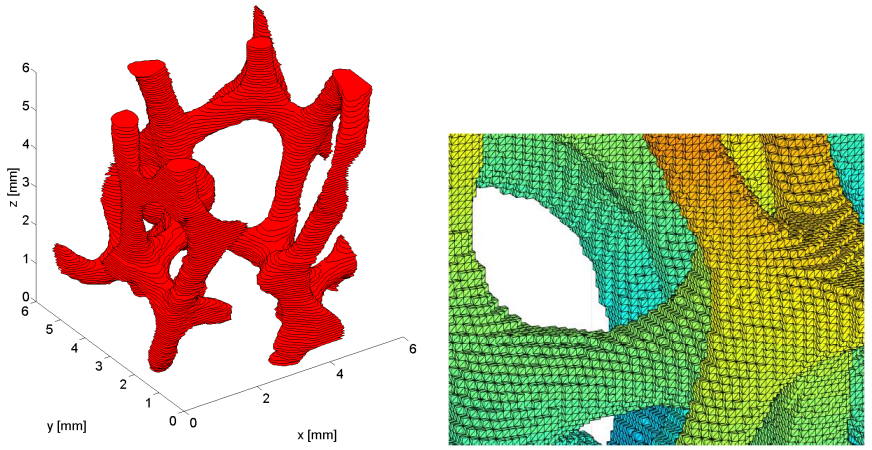

(a) Lattice Contours (b) Volumetric Pixels (VoXels) in CT Scan.

FIGURE 1.3. Contours per-slice and Voxels.

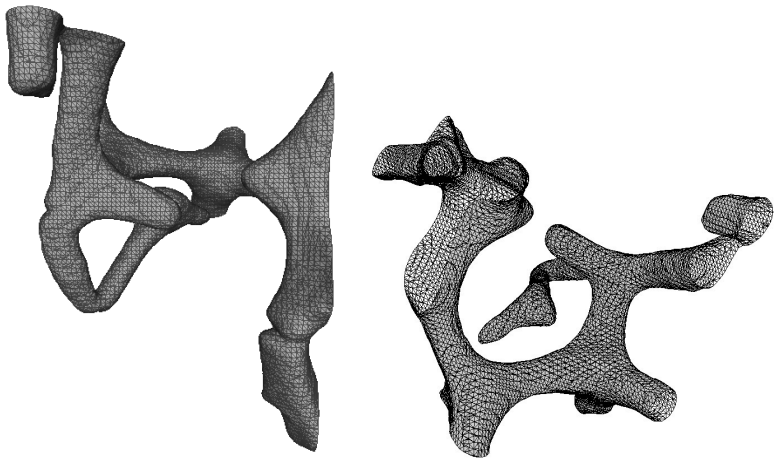

(a) View 1. (b) View 2.

FIGURE 1.4. Triangular Mesh Surfaces formed by Contour-mapping (generalized lofting [17, 11]) between Consecutive Cross Section Contour Sets.

(2) T triangulation approximating the iso-surfaces $V(p) = V_{TR}$ for $p \in \Omega$. Notice that $T = \cup_i T_{i,i+1}$.

The triangular mesh that materializes the mapping among contours of consecutive slices is calculated by algorithms discussed in [11] or [17] and produces the results in Fig. 1.4. The mapping among contours (i.e lofting) may have a strictly local proximity criterion (Voronoi - Delaunay methods, [17]) or it may have a topological and 2D - shape similarity rationale that selectively triggers the V-D methods ([11]). The topological and 2D shape similarity methods use the fact that

topological evolution of features along the cross sections obeys to only 3 topological transitions ([18]). A topological event corresponds to the addition of one of: 0-handle, 1-handle or 2-handle, to the previous contour, and causes the number of contours to change from cross section Π_i to cross section Π_{i+1}. Fig. 1.5 shows that the number of contours in slice Π_i will have a variation of +1, -1, +1, -1 as a consequence of the addition of 0-handle, 1-handle, 1-handle and 2-handle, respectively.

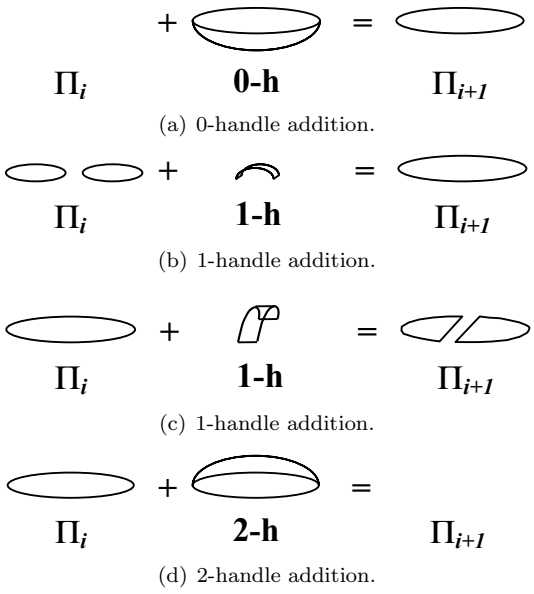

(a) 0-handle addition.

(b) 1-handle addition.

(c) 1-handle addition.

(d) 2-handle addition.

FIGURE 1.5. Topological Transitions as k-Handle Additions ([11]).

3.3. Triangular Mesh to Parametric Surfaces.

- **Given:**
  (1) T triangulation approximating the iso-surfaces $V(p) = V_{TR}$ for $p \in \Omega$.
- **Goal:**
  (1) A Set of parametric patches $S_j(u, w)$ which approximate the triangular mesh T so that $\cup_j S_j(u, w) \approx T = \cup_i T_{i,i+1}$.

In [19] an algorithm is reported, which uses the graph T under a point sample as proximity graph in Manifold Learning Algorithms. The parametric surfaces fit to the triangular mesh appear in Figs. 6(a) and 6(b).

4. Results and Discussion

4.1. Aluminium Foam geometrical modeling. Fig. 2(a) shows a slice of the CT scan, which corresponds to the pixels with $V(x, y, z) \geq V_{TR}$. The 2D boolean union of such pixels results in a city-block jagged boundary in Fig.2(b). If the distance between scan planes is considered, Volumetric Pixels (Voxels) are formed, which correspond to the parts of Ω filled by the Aluminum Foam (Fig.

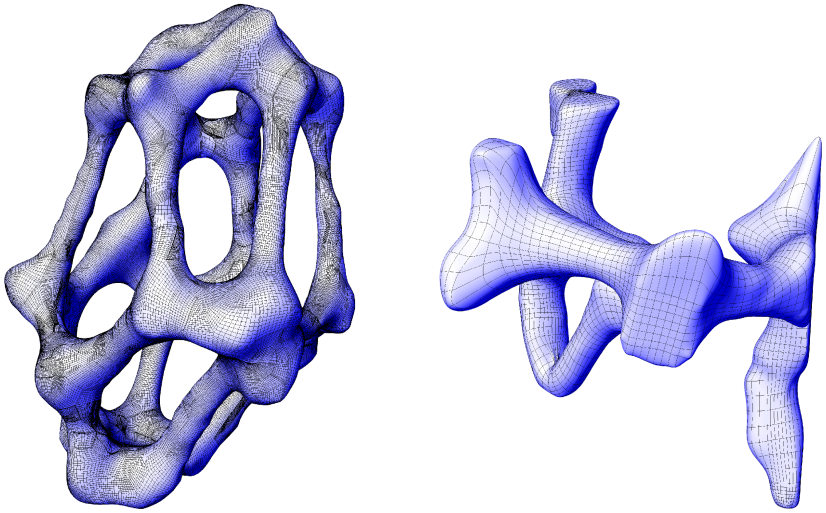

(a) Sub-domain (b) Surface Modeling of Subdomain.

FIGURE 1.6. Parametric surfaces of the geometric modeling of the aluminum foam.

3(b)). A smoothing of these jagged contours produced with a Catmull-Rom interpolation produces the results in Fig. 2(c). The collection of such cross sections for a particular neighborhood of Ω is shown in Fig. 3(a). The generalized lofting among cross sections produces triangular shells, shown in Fig. 1.4. The parametric surfaces fit to the triangular mesh appear in Figs. 6(a) and 6(b).

4.2. Experimental Set-Up. Consider a domain $\Omega \subset \mathbb{R}^3$ (Fig. 7(a)) open in the planes $z = 0$ and $z = L$ and closed in the sides (planes $x = 0$, $x = L$, $y = 0$, $y = L$). The boundary of the domain $\partial\Omega$, allows free pass of fluid in the planes $x = 0$ and $x = L$ and is hermetic in the planes $x = 0$, $x = L$, $y = 0$ and $y = L$. Ω is divided in 3 slices, as follows: (1) Ω_1, with $0 \leq z \leq \Delta_1$, filled with a viscous pore fluid. (2) Ω_2, with $\Delta_1 \leq z \leq \Delta_1 + \Delta_2$, filled with metallic foam whose interstices are filled by the fluid. (3) Ω_3, with $\Delta_1 + \Delta_2 \leq z \leq \Delta_1 + \Delta_2 + \Delta_3$, filled with the fluid. There are no obstacles for the movement of the fluid in the Z direction, except the presence of the aluminum foam itself.

At the plane $z = 0$ an acoustic wave excites the medium in direction perpendicular to the plane with an ultrasonic transducer. The wave is described in the frequency domain by a Gaussian distribution $\mathcal{N}(0, f_c)$. The value f_c will indicate whether the propagating wave is in Biot's high or low frequency domain, cf. discussion in [20]. It is of our interest to calculate Biot's high frequency limit, since the viscous effects of the fluid can be neglected, and the complexity of the constitutive equation of the fluid is significantly simpler. In order to enforce this, the value of the central frequency of the propagating wave must be significantly greater than

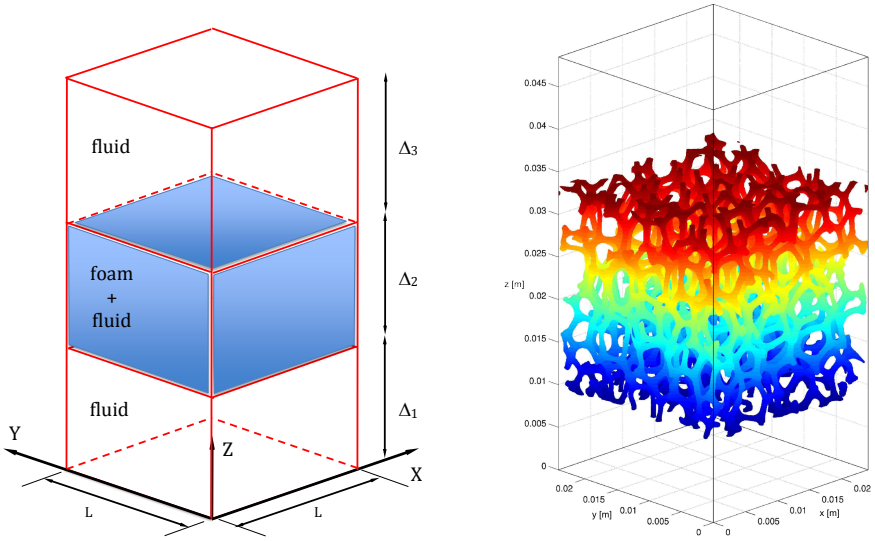

(a) Fluid and Foam-Fluid Domains Ω. (b) Foam Domain Ω_2

FIGURE 1.7. Experimental Set-Up

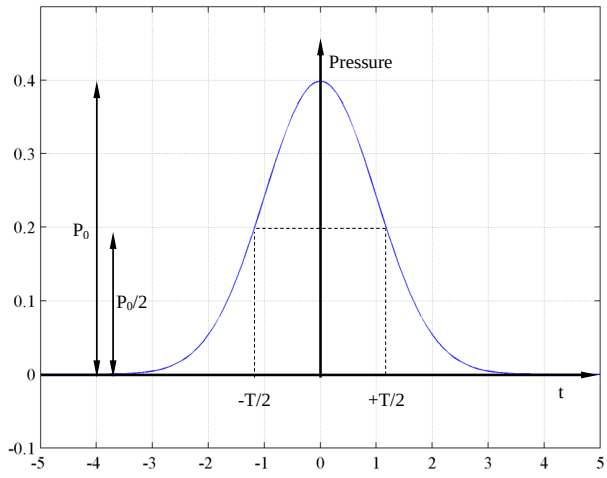

FIGURE 1.8. Pressure Wave

Biot's critical frequency. From this experimental set-up, two pressure waves are numerically obtained (slow and fast P-wave, cf. [21] , and then any missing material parameter in Biot's equation can be calculated (e.g. tortuosity).

$$f_{crit} = \frac{\eta}{\pi \rho^{fR} r^2} \tag{1}$$

The calculation of Biot's critical frequency f_{crit} is calculated using the pore radius r found from the parametric surfaces in section 3.3. It is found that f_{crit}

is smaller than 1 Hz. Therefore a wave with a central frequency of 24 KHz lies in the high frequency domain. To record the interaction of the wave with the water saturated foam, seismographs are placed in the planes $z = \Delta_1$ and $z = \Delta_1 + \Delta_2$. The material parameters for the water phase and the aluminum phase can be found in Tab. 1.1.

Young's modulus of aluminium	$E^s = 70.0$ GPa
Poisson number of aluminium	$\nu^s = 0.33$
Density of aluminium	$\rho^{sR} = 2700$ kg/m^3
Bulk modulus of water	$K^f = 1.48$ GPa
Density of water	$\rho^{fR} = 1000$ kg/m^3
P-wave velocity of water	$V_{p,water} = 1480$ m/s

TABLE 1.1. Modeling parameters of the fluid and solid phases

In order to simulate the experimental setup, the momentum equation is solved using a Rotated Staggered Grid Finite Differences scheme (RSG-FD)([22, 23, 24]). The RSG-FD method has proven to be an accurate approach to simulate the wave propagation phenomenon in porous media ([25],[26]). The geometric discretization is taken from the voxel data in section 3.2.1.

4.3. Water saturated aluminum foam simulation. Biot's theory ([21]) states that a wave propagating at high frequencies in a fluid saturated medium is constituted by two pressure waves and a shearing wave. Therefore it is expected that two P-waves can be measured using the first and second arrivals of the signal in the recorded data in the seismograms. It was only possible to measure a single P-wave from the seismographs, the other arrivals had excessive noise. Nevertheless, it was possible to view both propagating waves in the water saturated foam by digitally draining part of the foam and taking a snapshot when the wave was travelling through Ω_2. On Fig. 9(a), the aluminum foam phase has a faster propagating wave than that of the water phase. The measured velocity $V_{p,biot}$ is 1487 m/s.

4.4. Water saturated stiffened aluminum foam simulation. The simplification by Steeb ([27]) of Biot's equations leads to a single formula (2) where the pressure wave velocities can be calculated. All the material parameters necessary to calculate Biot-Willis' coefficients (i.e. N, A, Q, R, P and the density tensor $\hat{\rho}_{i,j}$) were measured with laboratory experiments except for the tortuosity. Therefore in order to calculate the tortuosity from the experimental setup, an additional simulation must be performed.

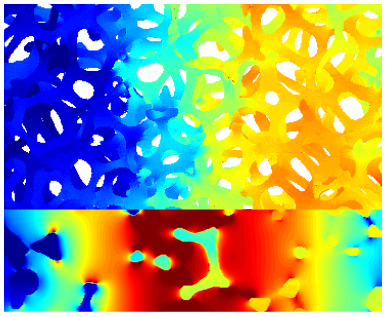

(a) Pressure wave snapshot in Ω_2. The camera is set perpendicular to the z-x plane.

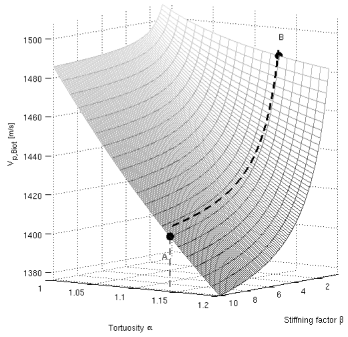

(b) Change in $V_{p,biot}$ as the aluminum foam is stiffened.

FIGURE 1.9. Pressure wave results for the stiffened and non-stiffened aluminum foam.

$$\xi_{1,2} = \frac{\Delta \pm \sqrt{\Delta^2 - 4(PR - Q^2)(\hat{\rho}_{11}\hat{\rho}_{22} - \hat{\rho}_{12}\hat{\rho}_{12})}}{2(PR - Q^2)},$$
$$\Delta = P\hat{\rho}_{22} + R\hat{\rho}_{11} - 2Q\hat{\rho_{12}}. \tag{2}$$

To circumvent the missing P-wave velocity problem, the aluminum foam is virtually stiffened with a parameter β. The effect of the stiffening parameter on $V_{p,biot}$ can be seen on Fig. 9(b). The density and Young's modulus of aluminum foam are multiplied by this parameter. This in turn doesn't modify the P-wave modulus of the aluminum phase, but it does create a very high impedance between the solid and fluid phase. The high impedance between the phases means that the wave will be mainly traveling through the water phase, and this allows to a very clear reading of the signals at the seismographs of $V_{p,biot}$.

The measured $V_{p,biot}$ for the stiffened aluminum foam setup is 1409 m/s. When comparing both results of $V_{p,biot}$ with the variance of the stiffening parameter β, and the tortuosity, it was found that the tortuosity of the aluminum foam is $\alpha_\infty = 1.14$.

We compare our results of tortuosity with the experimental results presented by Gueven et al. in [28] and [29] ($\alpha_\infty = 1.054$), finding that they match closely. From this we can verify that the proposed geometric model of the aluminum foam represents correctly the porous material sample.

We also compare our results with the values presented in [30], where the aluminum foam is modelled with a truncated tetrahedron. We find that geometrical modelling from micro-CT data give us more accurate information about the material properties than simplified models.

5. Conclusions and Future Work

The raw data of micro-CT data of an aluminum foam was successfully transformed from a scalar field in a regular grid in $\mathbb{R}^3$ to a watertight union of parametric surfaces $\cup_i S_i(u, w)$. From micro-CT based triangular mesh, it was possible to simulate the phenomenom of wave propagation in Biot's high-frequency domain. The parametric form of the mesh, $\cup_i S_i(u, w)$, allows to determine important geometric parameters used in Biot's equations (porosity, pore radius). Our geometric procedure was validated with simulations of wave propagation, and these closely resemble experimental results.

Future work includes the implementation of boundary elements, iso-geometrical analysis, calculation of additional macro-scale material properties and the intelligent automatic thinning of the cavernous system to achieve a graph - based node / beam representation.

Acknowledgment

The present work was supported by Ruhr-University, Germany, the CAD CAM CAE Laboratory, Universidad EAFIT, Colombia, and the Colombian Administration for Science and Technology (Colciencias). The authors thank Juan S. Ortiz, Jorge M. Patino and Diego Uribe for their expertise using RapidForm (TM) in the data quality control and exporting to FEA software.

CHAPTER 2

Estimation of large domain Al foam permeability by Finite Difference methods.

M. Osorno[1,2], H. Steeb[2], D. Uribe[1,2] and O. Ruiz[1].
[1] CAD/CAM/CAE Laboratory, Universidad EAFIT, Medellin, Colombia.
[2] Institute of Mechanics, Ruhr-University Bochum, Germany.

This research proposes a method to estimate the intrinsic permeability of porous media from geometry large data. The method was applied on a Packed spheres case and the comparison of the results with the Carman-Kozeny model presents a low error (5%). Subsequently the permeability of a micro-CT scanned sample of aluminum foam was estimated.
This research was made on collaboration between the Laboratory of CAD CAM CAE at Universidad EAFIT and the Institute of Mechanics at Ruhr-University Bochum. This article was presented on the Journal Proceedings in Applied Mathematics and Mechanics (PAMM). ISSN 1617-7061. Volume 13, Number 1, WILEY-VCH Verlag. December 2013. Pages 247-248. Editors: L. Cvetkovic, T. Atanackovic and V. Kostic.

Abstract. Classical methods to calculate permeability of porous media have been proposed mainly for high density (e.g. granular) materials. These methods present shortcomings in high porosity, i.e. high permeability media (e.g. metallic foams). While for dense materials permeability seems to be a function of bulk properties and occupancy averaged over the volume, for highly porous materials these parameters fail to predict it. Several authors have attacked the problem by solving the Navier-Stokes equations for the pressure and velocity of a liquid flowing through a small domain (Ω_s) of aluminium foam and by comparing the numerical results with experimental values (prediction error approx. 9%). In this article, we present calculations for much larger domains (Ω_L) using the Finite Difference (FD) method, solving also for the pressure and velocity of a viscous liquid flowing through the Packed Spheres scenario. The ratio $Vol(\Omega_L)/Vol(\Omega_s)$ is around 10^3. The comparison of our results with the Packed Spheres example yields a prediction error of 5% for the intrinsic permeability. Additionally, numerical permeability calculations have been performed for Al foam samples. Our geometric modelling of the porous domain stems from 3D X-ray tomography, yielding voxel information, which is particularly appropriate for FD. Ongoing work concerns the reduction in computing times of the FD method, consideration of other materials and fluids, and comparison with experimental data.

1. Introduction

Permeability is an important property in the design of filters of metallic foam, porous implants and other applications that require a flow through a porous medium ([31]). In this article we estimate the permeability of high porosity Aluminium foam ($\phi > 0.8$) employing the Finite Difference method . For the numerical calculation of permeability of metallic foams the following methods have been applied: (1) Finite Volumes, (2) Lattice Boltzmann, (3) Finite Difference method. Gerbaux et al. ([32]) calculate the permeability of 3 real metallic foams by solving fluid flow in the porous medium with the Lattice Boltzmann method and the finite Volume Method. Xu et al. ([33]) perform a finite volume analysis to estimate the permeability of some foams with different porosities and foam cells properties.

Petrasch et al. ([34]) determine effective porous media properties such as porosity and permeability from a digital representation of reticulate porous ceramics generated by X-ray tomographic scans. Nabovati et al. ([35]) calculate the permeability for fibrous porous media in a wide range of porosity by applying Darcy's law.

So far, only small domains of high porous materials like metallic foams have been numerically analyzed. Especially in X-ray images based investigation, the question arises is such domain one representative elementary volume? Therefore, we propose a numerically efficient FD scheme on cartesian grids which is higly compatible with 3dim CT images.

2. Methodology

We propose a straightforward method to calculate permeability of porous media: (I) Discretization of equations (3) and (5) on a staggered grid by using a 2nd order FD method with periodic boundary conditions for velocity in the inlet and outlet of the channel (Fig. 2.1). (II) Solution of the resulting equation system with the iterative Gauss-Seidel scheme. The Gauss-Seidel method does not require to

store a coefficient matrix. (III) Calculation of the volume averaged velocity u_m from the velocity field computed in step 2. (IV) Estimation of the medium permeability with Darcy's law (Eq. 14). The notation used is: k^s: intrinsic permeability according to Darcy's law, μ: dynamic viscosity, u_m: volume averaged velocity in flow direction in the free volume, Δp: pressure drop in flow direction,

$$\nabla p = \mu \nabla^2 \mathbf{u}, \tag{3}$$

$$\nabla \cdot \mathbf{u} = 0, \tag{4}$$

$$\nabla \cdot \nabla p = 0, \tag{5}$$

$$u_m = \frac{\int_{V_f} |u_z| dv}{V_f}, \tag{6}$$

$$k^s = \frac{\mu u_m}{\Delta p}. \tag{7}$$

2.1. Method Validation. The method was validated with a regular packed sphere case in 3D (Fig. 2(a)) whose permeability can be calculated with the Carman-Kozeny model proposed in [36] (Eq. 8) and with the Rumpf-Gupte model proposed in [37] (Eq. 16). The notation used is: k^s_C: permeability by Carman-Kozeny model, k^s_R: permeability by Rumpf-Gupte model, d: sphere diameter and ϕ: porosity. The relative error between the estimated permeability for a regular pack of spheres in a channel with 10 spheres in direction Z ($Sph_z = 10$) and the Rumpf-Gupte model is 5.5% ,

$$k^s_C = \frac{\phi^3}{180(1-\phi)^2} d^2, \tag{8}$$

$$k^s_R = \frac{\phi^{5.5}}{5.6} d^2. \tag{9}$$

3. Results

The permeability of an aluminium foam was estimated for a domain of 24 mm $\times$ 24 mm $\times$ 24 mm (400 $\times$ 400 $\times$ 400 voxels). Figure 2(b) shows the velocity in Z direction on plane YZ at x= 12mm. The calculated results for this case are $u_m = 6.5093 \times 10^{-9}$ m/s and $k^s = 7.7967 \times 10^{-7}$ m^2. Our implementation allows to compute 256×10^6 degrees of freedom with a single processor.

4. Conclusions and Future work

The permeability of a lattice of aluminium foam was calculated with Darcy's law, using Finite Difference methods to simulate a viscous flow through a porous medium. The proposed method optimizes memory usage, therefore it allows to simulate large domains in single processors. Future work includes the reduction in computing time, the modification of flow parameters such as the input flux and the estimation of the permeability of materials with different porosities.

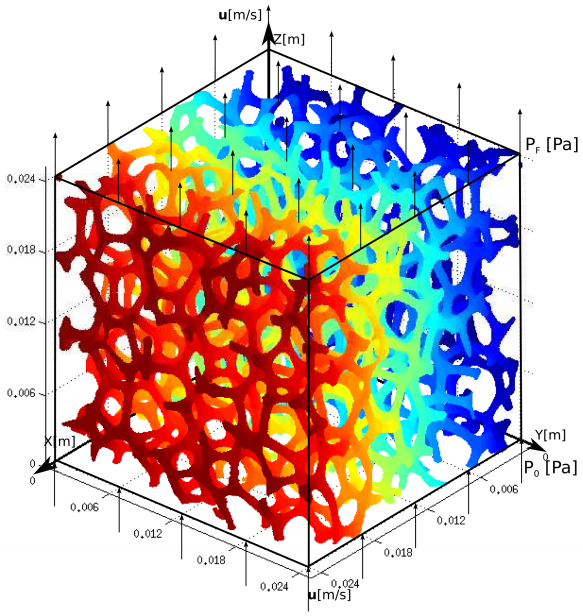

FIGURE 2.1. Domain $400 \times 400 \times 400$ voxels (24mm $\times$ 24mm $\times$ 24mm).

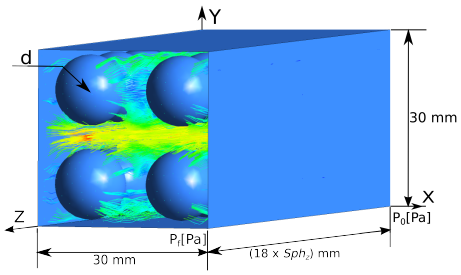

(a) Regular packed sphere case

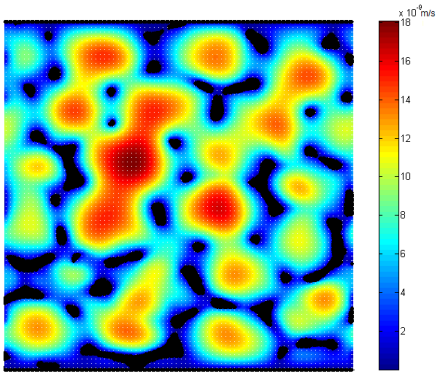

(b) Velocity in Z direction on plane YZ at x= 12mm.

FIGURE 2.2. Numerical estimation results.

CHAPTER 3

Finite difference estimation of permeability in large domains in a wide porosity range.

M. Osorno[1,2], H. Steeb[2], D. Uribe[1,2] and O. Ruiz[1].
[1] CAD/CAM/CAE Laboratory, Universidad EAFIT, Medellin, Colombia.
[2] Institute of Mechanics, Ruhr-University Bochum, Germany.

Permeability is an important property in the analysis of flow through porous materials. This research proposes a workflow to estimate the permeability of porous materials in a wide range of porosities $[0.146 - 0.934]$**. A parallel solver is proposed to simulate a Stokes flow through porous media from the micro-structure of the material. The averaged pressure and velocity fields calculated are used to calculate the permeability from Darcy's law.**
This research was made on collaboration between the Laboratory of CAD CAM CAE at Universidad EAFIT and the Institute of Mechanics at Ruhr-University Bochum. This paper is waiting for submission to Journal Archive of Applied Mechanics. ISSN: 0939-1533. Publisher: Springer Berlin Heidelberg. Authorization for submission by Ruhr-University Bochum is pending.

Abstract. Numerical calculation of effective hydro-mechanical properties of porous media is relevant in geophysics, manufacturing, bio-mechanics and environmental sciences, among other fields. Because of the dependency of effective physical properties (e.g. elastic moduli and permeability) on morphological details on the pore scale such as shape and size of pores and cracks and with respect to large necessary representative volume elements, numerical simulation techniques have to be optimized on order to obtain reliable results. The current state of the art in the field of such numerical investigations of effective permeability of porous materials, based on Lattice-Boltzmann, Finite Volumes, Explicit Jump Stokes methods still presents limitations in the size of the analyzed domain. In response to these shortcomings, we propose an efficient and reliable method to calculate the intrinsic permeability of porous materials directly from voxel-based data obtained from imaging techniques like X-ray microtomography. We implement a parallel Finite Differences solver, allowing the calculation of large domains. We test our method in a diverse selection of materials, obtaining accurate results for a range of porosities, wider than the ranges previously reported. Ongoing work includes the estimation of other effective properties of porous media.

Glossary

$\mathbf{u}$	Velocity. [m/s]
d_s	Sphere diameter. [m]
$k_C^{\mathfrak{s}}$	Permeability (Carman-Kozeny, spheres array). [m^2]
$k_D^{\mathfrak{s}}$	Permeability (Darcy's law).[m^2]
$k_R^{\mathfrak{s}}$	Permeability (Rumpf and Gupte, spheres array). [m^2]
$k_T^{\mathfrak{s}}$	Permeability (Poiseuille flow, capillary tube). [m^2]
p	Pressure. [Pa]
r_t	Radius of capillary tube. [m]
u_m	Volume averaged velocity. [m/s]
Δp	Pressure drop in the medium. [Pa/m]
$\eta^{\mathfrak{f}R}$	Dynamic viscosity.[Pa s]
ϕ	Porosity of the material.
Ω	Domain of investigated material in $\mathbb{R}^3$.

1. Introduction

Experimental estimation of properties of porous materials is an expensive and time consuming process. Because of these expenses, their numerical estimation is becoming increasingly used, presenting several advantages: (1) only one material sample is needed for the estimation of numerous properties, (2) CT-scan digitization takes relatively short time, and (3) variables that in real experiments are hard to maintain (e.g. room temperature) are controllable. In this article we focus in the estimation of Intrinsic Permeability as defined in Ref. [38]. For the sake of brevity we shall use Permeability to mean Intrinsic Permeability.

Permeability is a critically relevant property affecting flow through porous media and it is strongly dependent on the geometry of the porous media. In order to sample the medium, some authors use industrial Computer Tomography (CT) scans. In other cases the media geometry is generated artificially. In the present investigation we work with both kinds of geometric models. Our artificial geometry

is generated as a voxel-based image, therefore emulating the CT-scan format.

One of the main difficulties in the estimation of effective properties of porous media from the micro-structure information, is the simulation of domains large enough to be representative for the material. Several authors have proposed to divide the domain and calculate the effective property as the average of the results obtained in the subdomains. The averaging method arises problems because the obtained results depend on the domain size and the chosen subdomains. In this article we propose a method that allows to calculate large domains, avoiding variations in the estimated permeability because of the domain size.

The proposed workflow begins from a voxel-based geometry obtained directly from the image segmentation of a CT-scanning. We estimate the permeability as follows: (1) Set-up of boundary value problem, (2) Parallel computing of Stokes flow implementing the Finite Difference (FD) method, and (3) Estimation of Darcy permeability from the velocity and pressure field calculated in the previous step. We prove our method with pervious and semipervious materials, in a range of porosities from 0.146 to 0.934.

Section 2 presents a literature review about existent numerical methods for permeability calculation. Section 3 discusses the proposed methodology: geometry pre-processing, setting of boundary value problem, parallel computation and permeability calculation. Section 4 displays the estimated permeability for the analyzed geometries. Section 5 presents conclusions and future work.

2. Literature Review

Ref. [32] calculates the permeability of three metallic foams by solving the pressure and velocity in the porous medium with the Lattice Boltzmann and the Finite Volume methods. This work combines micro-tomography - based geometric modelling with numerically solved transport equations to estimate domain-averaged foam permeability. The authors report that the estimated permeability variates with the domain size, given that is not large enough to represent the material.

Ref. [39] numerically estimates the permeability for a three-dimensional sample of Fontainebleau stone obtained from tomography scans, applying the Finite Difference and Latice-Boltzmann methods. Comparing the two methods applied the authors conclude that the FD method has a lower requirement of memory by a factor of 2.5. The permeability computed for the Fontainebleau stone is compared with the estimated permeability of two stochastic models with the same porosity and specific surface area as the digitized sample of the Fontainebleau stone. According to the results of [39] it is possible to conclude that for obtaining accurate results of permeability is necessary to use the actual, and more complex, digitized model.

Ref. [40] calculates some effective properties of porous media (Fontainebleau sandstone, Berea sandstone, carbonate sample and sphere pack), including the absolute permeability. This property is calculated from segmented 3D images, applying

Lattice-Boltzmann and Explicit jump Stokes methods for simulation of the flow through the media. The model size causes variations in the obtained results.

Ref. [33] estimates (via Finite Volume Analysis) the permeability of foam cells with high porosities. Its method presents the limitation of only addressing small periodic domains. Ref. [41] reports the flow simulating in periodic cells of porous media by solving the Navier-Stokes equations in a control volume by employing pressure correction and an unstructured mesh topology. The methods presented in Refs. [33] and [41] were only tested with materials with high porosity.

Ref. [34] determines porous media properties such as porosity and permeability starting with X-ray tomographic scans. The proposed method is applied in reticulate porous ceramics, but it can be applied in any porous structure that admits tomographic samples. For the calculations was necessary to generate a tetrahedrical mesh.

One of the main difficulties in the estimation of effective properties for porous materials (in this case, permeability) is the simulation on domains large enough to be considered representative. A common shortcoming found is that the methods proposed by the different authors are only tested in a narrow range of porosities. In response to the presented problems, this article implements a method to estimate permeability for large domains of diverse kind of materials (low and high porosity).

3. Methodology

The aim of the present contribution is to present a workflow for an efficient numerical calculation of intrinsic permeabilities of low- and high-porous materials. Therefore we choose representative examples of such media from sandstones ($\phi = 0.146$) high porous man-made metal foam ($\phi = 0.935$). We restrict ourselves on stationary flow processes on the pore-scale leading to a creeping flow process on the up-scaled macroscopical scale.

The starting point of our workflow is a segmented binary 3-dim voxel-based data set obtained e.g. from X-ray synchrotron or desktop microtomography. A discussion about the important step from the reconstructed tomographic raw data to the binarized data set is out of the focus of the paper, cf. [42]. On basis of the cartesian grid of the voxel data, we perform the Finite Difference Stokes analysis.

The averaged velocity and pressure fields numerically calculated are employed in Darcy's law to estimate the permeability. In this section we described the proposed workflow (See Fig. 3.1):

(1) Geometry pre-processing for domains that present disconnected cavities, (2) Set-up of boundary value problem (Stokes flow simulation) (3) Computation of velocity and pressure field, and (4) Calculation of permeability.

3.1. Geometry Pre-processing (1). Some domains, specially ones with low porosity, present disconnected cavities. Those cavities do not affect the flow patterns, since no liquid reaches them. However, they affect the volume averaging of

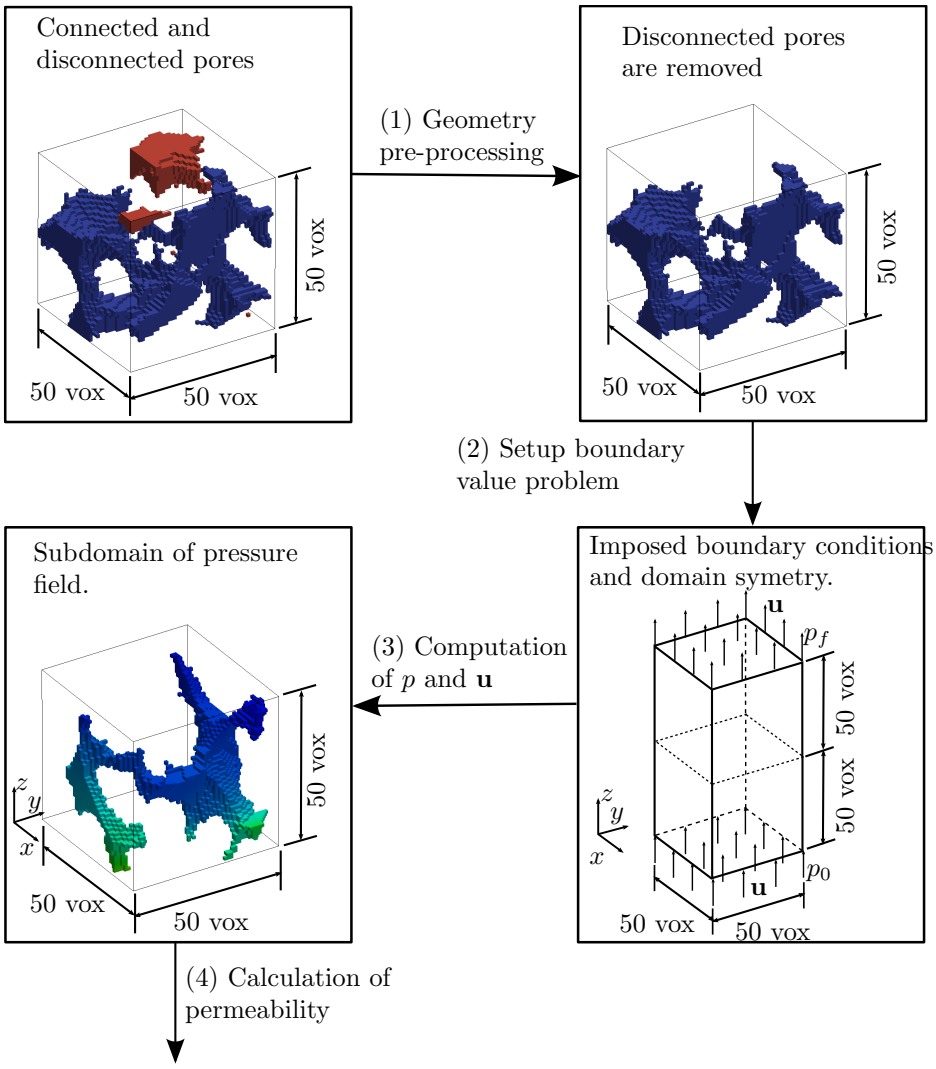

FIGURE 3.1. Workflow for intrinsic permeability calculation

the velocity field (Sec. 3.4) and consume computing time. Therefore they must be eliminated from the domain geometry before the computation starts. These disconnected cavities are indirectly identified by applying a seed region growth algorithm. Fig. 3.2 shows a subdomain of the Fontainebleau stone cavities. The connected domain network is displayed in pink color, while the disconnected one appears on blue color.

3.2. Set-up of boundary value problem (2). We simulate a Stokes flow (stationary, incompressible flow with Re$\ll$ 1) through a porous media. This is governed by the Eqs. 10 and 11:

$$\nabla p = \mu \nabla^2 \mathbf{u} \tag{10}$$

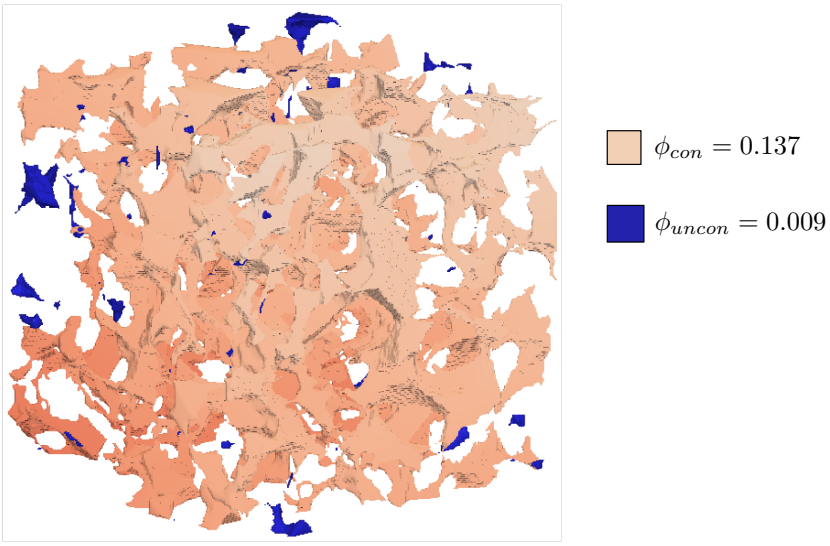

FIGURE 3.2. Geometry model of Cavity Network (pink) and Isolated Cavities (blue) in Fontainebleau Stone.

$$\nabla \cdot \mathbf{u} = 0 \tag{11}$$

By applying the divergence operator in both sides of the Eq. 10 we obtain:

$$\nabla \cdot \nabla p = 0 \tag{12}$$

To solve the velocity and pressure fields, the boundary value problem is posed onto a digitized sample of the porous material as follows: The porous media is enclosed in a rectangular prismatic domain $\Omega \subset \mathbb{R}^3$. The planes $x = 0$, $x = L$, $y = 0$ and $y = L$ are closed walls, and no-slip boundary conditions are applied. Periodic boundary conditions are applied in the velocity field ($\mathbf{u}(z = 0) = \mathbf{u}(z = L)$). The boundary conditions of the pressure field are defined by a constant function in the planes $z = 0$ and $z = L$ ($p(z = 0) = p_0$, $p(z = L) = p_f$). The domain Ω no occupied by the porous media is filled with a fluid with high viscosity and assumed incompressible. Fig. 3.3 shows the domain setup for some of the porous media analyzed.

In order to impose the periodic boundary condition for the velocity field in non-periodic porous media (e.g. Aluminium foam, Fontainebleau sandstone), we generate a mirror of the domain relative to the plane $z = L/2$.

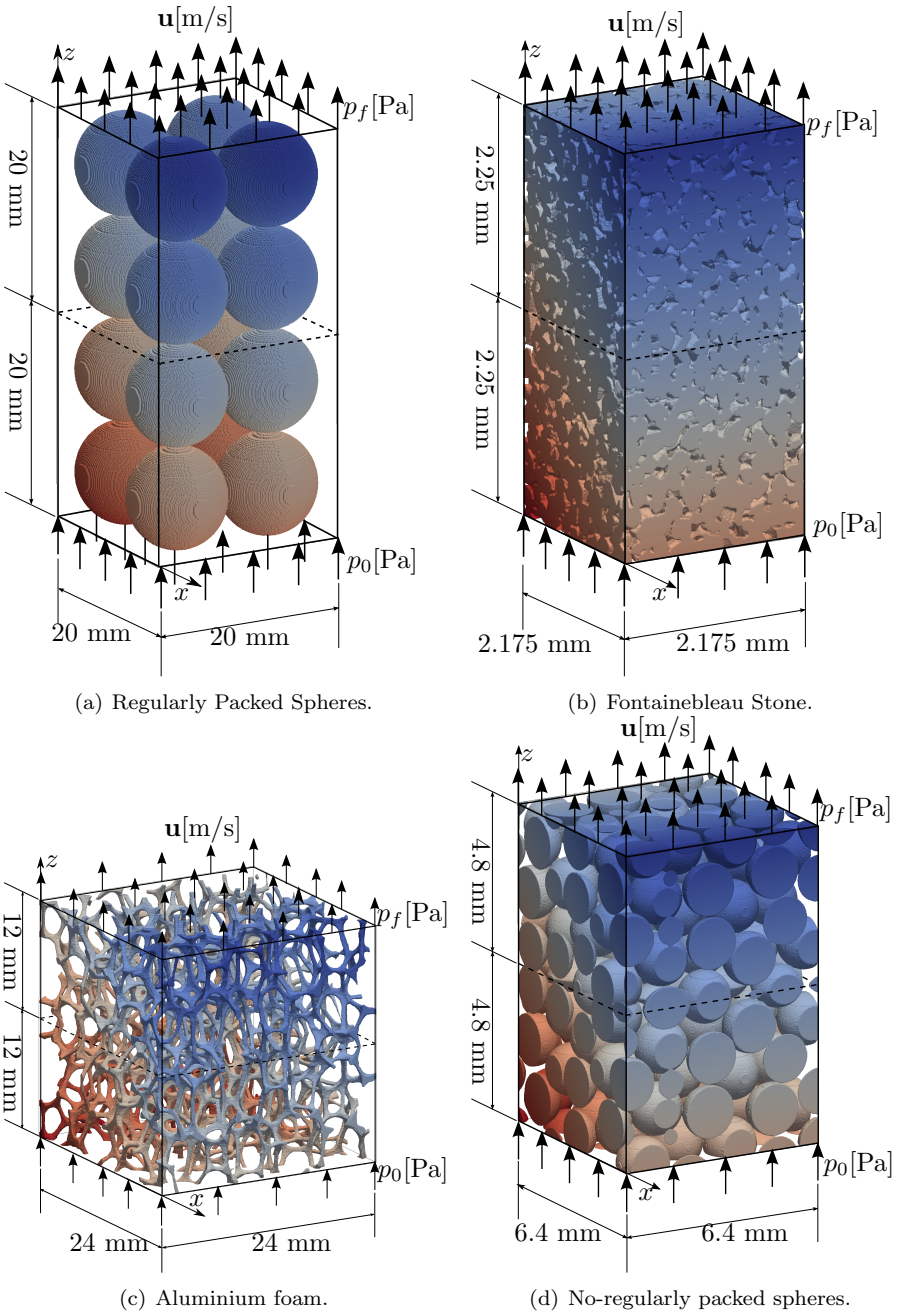

(a) Regularly Packed Spheres.

(b) Fontainebleau Stone.

(c) Aluminium foam.

(d) No-regularly packed spheres.

FIGURE 3.3. Domain setup of porous media analyzed

3.3. Computation of u and p (3). Eqs. 10 and 12 are discretized on a regular staggered grid ([43]) using second order FD method. Fig. 3.4 shows a 2d example of the discretization for visualization purposes. A regular grid allows to use the geometry information directly from the scan data, thus avoiding: (1) loss

of information of the geometry, and (2) spending of computational resources in the generation of geometrical representations such as triangulations or parametric surfaces.

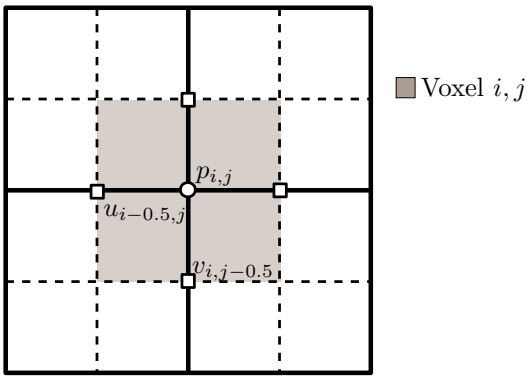

FIGURE 3.4. Example in 2d of discretization of pressure and velocity field.

The resultant system of linear equations is solved by applying the iterative Succesive Over-Relaxation method SOR ([44]). We used a relaxation factor $\omega = 1.2$ for a faster convergence.

Digitization of porous materials samples with the use of CT-scanners gives as a result massive quantities of data. We look to be able to compute those extremely large domains avoiding memory problems, therefore we implemented our own solver in parallel computation. The implemented solver can run in few desktop computers (without demanding specifications) connected in parallel, but if desired can also be used in a super-computer. Both cases were tested with good performance results.

Given the advantage of using distributed memory in our problem, we parallelized the computation using MPICH2 (Message Passing Interface based on Chameleon portability system). The domain was divided between the processes in a straightforward way. We split the domain with a family of equidistant planes, normal to the Z axis, according to the number of cores used. Fig. 3.5 shows an example of the domain division proposed for the code parallelization.

In parallel computation the communication among processes represents a resources-consuming task. We minimize this communication expense by having each process to pass to the neighboring one only a slice of the domain (gray voxels in Fig. 3.5). The communication operations were organized in a ring network ([45]), where we can find a communication link between the first and last process.

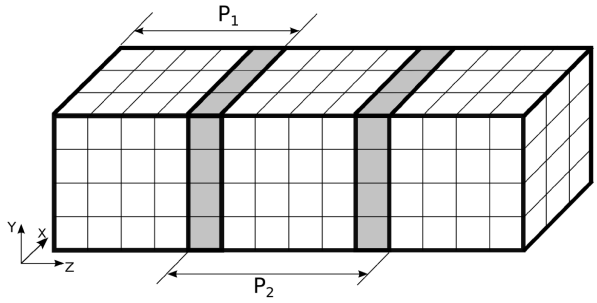

FIGURE 3.5. Example of domain division for parallelization. Voxels P_1, P_2,..., are processed in parallel. Voxels common among processes appear in grey color.

Fig. 6(a) shows a $\mathcal{O}(N)$ relation between the size of the domain (number of elements) and the time (seconds) that takes each iteration. Fig. 6(b) shows how the time per iteration decreases as the number of processors increases (for a domain of 400^3 voxels).

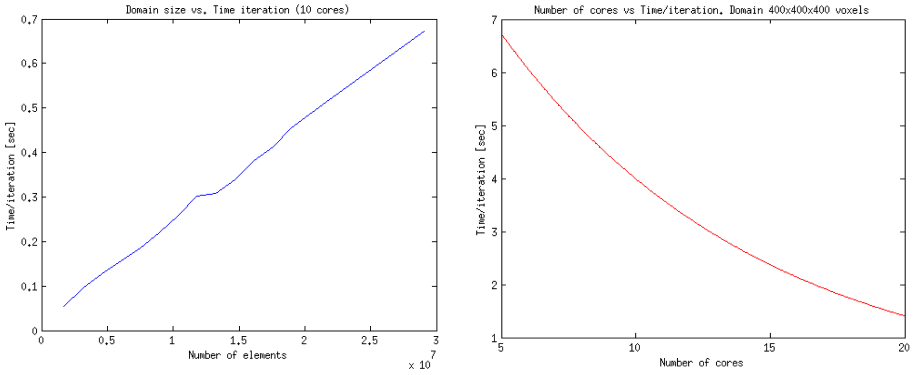

(a) Time per iteration as a linear function of domain size.

(b) Time per iteration as function of the number of processors used.

FIGURE 3.6. Parallelization

The number of iterations needed for convergence is directly affected for the domain size and the porosity of the studied material. The upper bound of the implemented SOR method is $\mathcal{O}(N/p)$, where N is the elements number and p the number of processors used.

3.4. Calculation of permeability (4). From the velocity and pressure field calculated in the previous section (Sec. 3.3) we calculate Δp (imposed boundary condition) and the volume average velocity (Eq. 13).

$$u_m = \frac{\int_{V_f} |u_z| dv}{V_f} \tag{13}$$

The porous media intrinsic permeability is calculated from Darcy's Law ([46]) (Eq. 14).

$$k_D^s = \frac{\mu u_m}{\Delta p} \tag{14}$$

4. Results and Discussion

Tab. 5.1 shows a summary of the obtained results for the different materials studied. It can be seen a comparison between the reference and calculated values of permeability, showing the accuracy of the method. Tab. 5.1 also shows the dimension of the domain simulated and the range of porosities in which our method was proved. For benchmark purposes, we present results for domains smaller than the largest possible with our method.

Case	Ref. Value	Sample size [Vox]	ϕ	$\sum$ Voxels	$\sum$ Vox in pore space	Reference k^s [m^2]	Calculated k_D^s [m^2]
Al foam	No ref.	$400 \times 400 \times 400$	0.935	64×10^6	59.87×10^6	–	7.8124×10^{-7}
Capillary tube	Ref. [47]	$100 \times 100 \times 400$	0.785	4×10^6	3.14×10^6	9.8175×10^{-6}	9.6316×10^{-6}
Regularly packed spheres	Ref. [37]	$200 \times 200 \times 400$	0.414	16×10^6	6.62×10^6	1.3955×10^{-9}	1.0867×10^{-9}
No-Regular packed spheres	Ref. [40]	$400 \times 400 \times 600$	0.343	96×10^6	32.92×10^6	2.6668×10^{-10}	2.1985×10^{-10}
Fontainebleau stone	Ref. [40]	$290 \times 290 \times 600$	0.146	50.46×10^6	7.36×10^6	1.8765×10^{-12}	9.6982×10^{-12}

TABLE 3.1. Results summary of the analysed materials.

4.1. Aluminium Foam Permeability. The permeability was estimated in a high porosity medium in a domain of 400^3 voxels (256×10^6 DOF). The results can be seen in the Tab. 5.1. There is no reference value for this material permeability. Fig. 3.7 shows the stream lines of the simulated flow through the aluminium foam.

4.2. Flow through a capillary tube. A Stokes flow was simulated through a capillary tube with ratio length/radius = 4. The estimated permeability, applying the proposed method, presents an error of 1.89% respect to the analytical solution (Eq. 15) presented in [47], Fig. 3.8 shows the profile of the velocity in z direction for the simulated and analytical solution. The numerical results are shown in the Tab. 5.1.

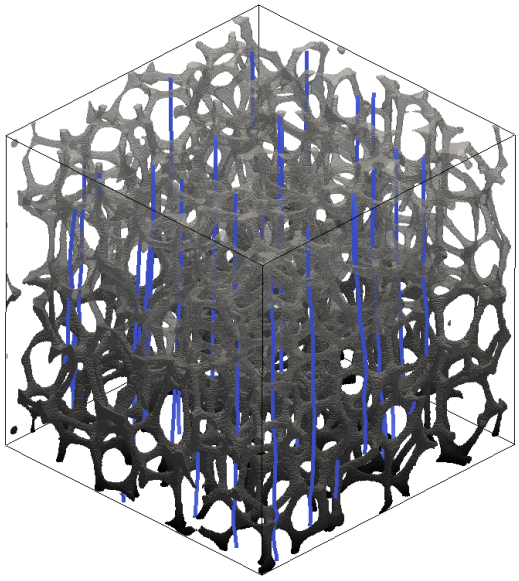

FIGURE 3.7. Aluminium foam domain. Chosen computed streamlines.

$$k_T^s = \frac{\pi}{32} r_t^2 \tag{15}$$

4.3. Regularly packed spheres. Tab. 5.1 shows the estimated permeability for a regular packed sphere array ($d_s = 10$ mm) with porosity of 0.4139 vs. the reference value of the permeability calculated with the model proposed Rumpf and Gupte in [37] (Eq. 16) for spheres of diameter 10 mm. Fig. 3.9 shows the stream lines for the calculated velocity field.

$$k_R^s = \frac{\phi^{5.5}}{5.6} d_s^2 \tag{16}$$

4.4. No-Regular packed spheres. We calculate the permeability for the domain of packed spheres ($\phi = 0.343$) proposed in [40] and compare our results with the benchmark values given by Andra et al. Fig. 3.10 shows a subdomain of the no-regular packed spheres, the top shows the magnitude of the velocity field, and the bottom shows the domain geometry. The calculated and reference values can be seen in Tab. 5.1.

4.5. Fontainebleau Stone. To prove our method with a low porous material, the permeability of the Fontainebleau stone ($\phi = 0.146$) is calculated and compared with the benchmark value in [40]. Fig. 3.11 shows a subdomain of the Fontainebleau stone, in the top can be seen the magnitude of the velocity field calculated, and in the bottom of the piece can be seen the geometry. Tab. 5.1 shows

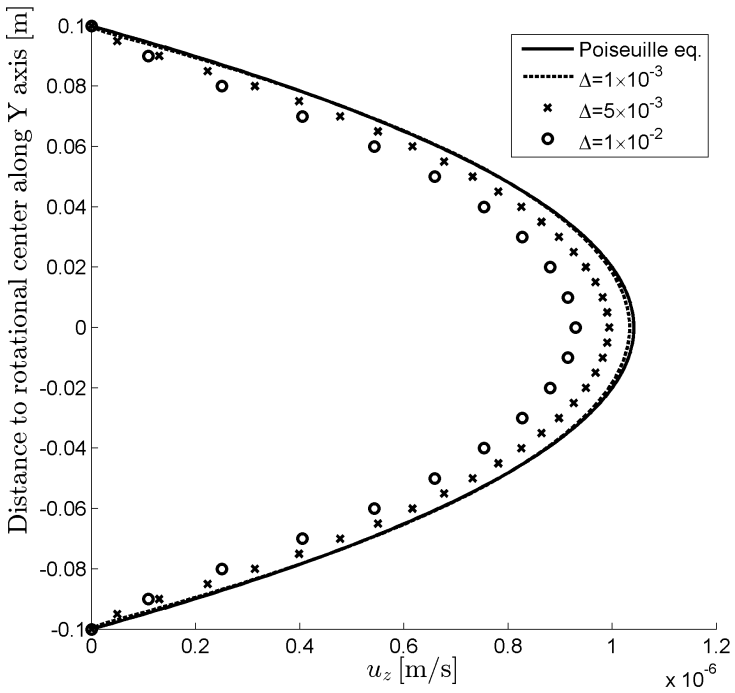

FIGURE 3.8. Profile of flow velocity in capillary tube. Comparison of Poiseuille equation with simulation with different discretizations.

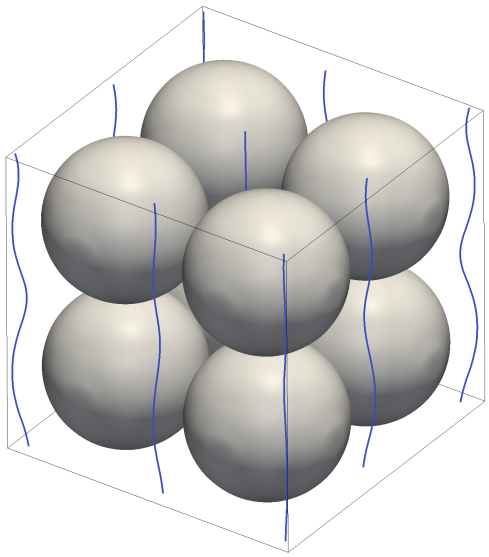

FIGURE 3.9. Regularly packed spheres domain. Chosen streamlines

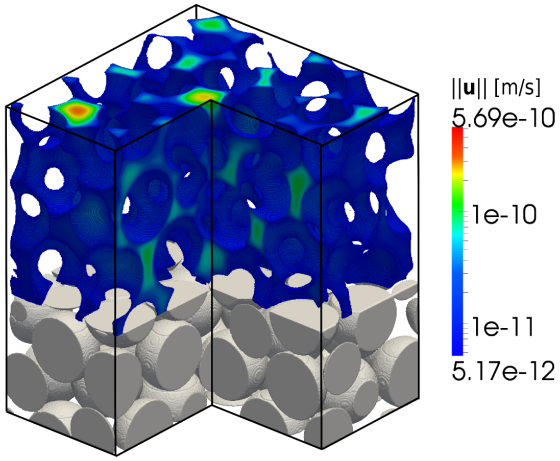

FIGURE 3.10. Subdomain of irregularly packed spheres. Top: Magnitude of fluid velocity. Bottom: Geometry.

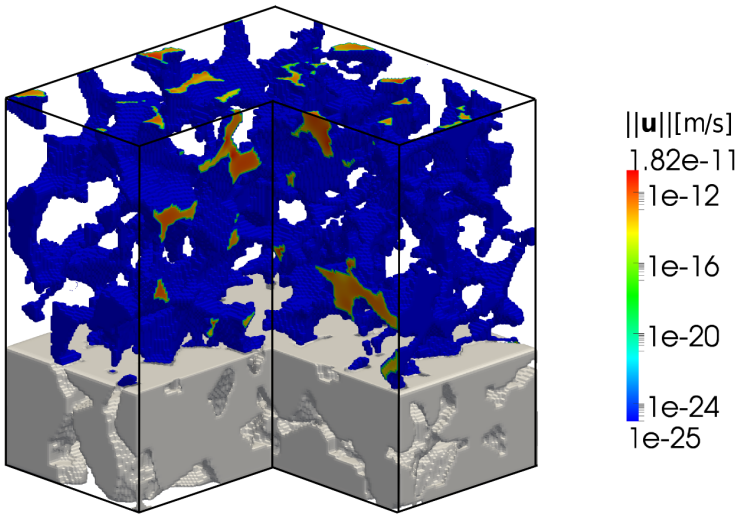

FIGURE 3.11. Sub-domain of Fontainebleau Stone. Top: Magnitude of fluid velocity. Bottom: Geometry.

the calculated permeability and the reference value.

We found in the calculated velocity field the existence of divergence in the connection between a pore and pore throat, when the throat diameter is relatively much smaller than the pore diameter (Fig. 3.12). This kind of connection occurs mainly in materials with low porosities.

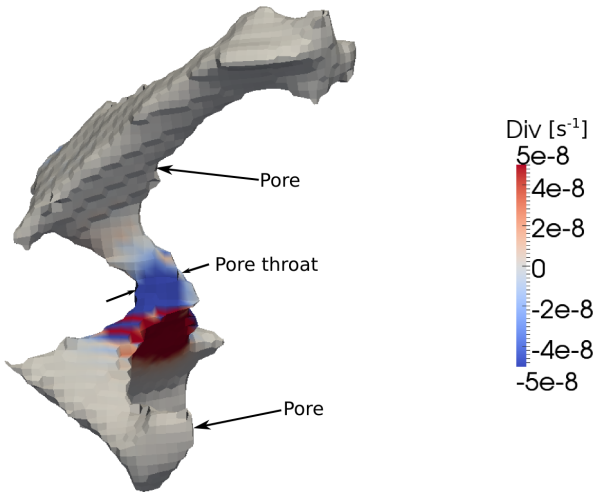

FIGURE 3.12. Divergence of velocity field in subdomain of Fontainebleau stone

In our simulations are applied boundary conditions that assure a viscous regime in most of the flow domain, but in these specific connections we found that inertial effects are dominant. Even with this error source, we found that the calculated value of permeability presents a low error respect to the reference value and a solver that includes inertial forces is not needed.

5. Conclusions and future work

The permeability was estimated for a set of materials which porosities $\phi \in [0.146, 0.935]$. A source of error found for the permeability calculations is the existence of divergence in the velocity field because of the sharp changes in the material pores diameter and small pore throats relative to the pore size. This is more common in the materials with low porosity.

Our method demands low computational resources, making possible to calculate large domains in desktop computers connected in parallel, but if needed can also be employed in a super-computer.

Future work includes the estimation of effective properties of porous materials such as the tortuosity and the comparison of the proposed method against other numerical methods such as Lattice-Boltzmann.

Acknowledgements

The present work was supported by Ruhr-University, Germany, the CAD CAM CAE Laboratory EAFIT, Colombia, and the Colombian Administration for Science and Technology (Colciencias). M. Osorno thanks Colciencias and the program *Jovenes investigadores*.

CHAPTER 4

Numerical estimation of carbonate properties using a digital rock physics workflow

M. Osorno[1], D. Uribe[2], E.H. Saenger[3], C. Madonna[3], H. Steeb[2] and O. Ruiz[1]
[1] CAD/CAM/CAE Laboratory, Universidad EAFIT, Medellin, Colombia.
[2] Institute of Mechanics, Ruhr-University Bochum, Germany.
[3] Geological Institute, ETH Zürich, Switzerland.

Numerical estimation of effective properties of porous media is possible from digitized samples. The image segmentation realized to the scanned data affect the estimation of the porous media properties. In this paper is proposed an image segmentation procedure. The method is applied to a Carbonate digitized sample to calculate p-wave velocity and permeability.
This research was made on collaboration between the Laboratory of CAD CAM CAE at Universidad EAFIT, the Institute of Mechanics at Ruhr-University Bochum and the Geological Intitute at ETH Zürich. This paper was accepted on the Conference EAGE. Amsterdam, Netherlands. Date: June-2014

Abstract. Digital rock physics combines modern imaging with advanced numerical simulations to analyze the physical properties of rocks. In this paper we suggest a special segmentation procedure which is applied to a carbonate rock from Switzerland. Starting point is a CT-scan of a specimen of Hauptmuschelkalk. The first step applied to the raw image data is a non-local mean filter. We then apply different thresholds to identify pores and solid phases. Because we are aware of a non-neglectable amount of unresolved micro-porosity we also define intermediate phases. Based on this segmentation determine porosity-dependent values for the p-wave velocity and for the permeability. The porosity measured in the laboratory is then used to compare our numerical data with experimental data. We observe a good agreement. Future work includes an analytic validation to the numerical results of the p-wave velocity upper bound, employing different filters for the image segmentation and using data with higher resolution.

1. Introduction

Three-dimensional (3D) information on rock micro-structures is important for better understanding physical phenomena as well as for rock characterization at the micro-scale ([48]). The most common non-destructive 3D imaging method for earth sciences is X-ray computed tomography (CT). A common problem, however, is a clear trade-off between sample size and resolution. For each material sample, it has to be clarified if the chosen sample size is representative for the physical property to be computed. In addition to a purely geometrical characterization of the material, the digitized samples allow to calculate effective physical properties of the porous material like elastic parameters, permeability, electric conductivity, etc. However an accurate result of the estimated properties is dependent on factors such as the digitization resolution and the ratio domain size vs. pore size. This last factor must be large enough to make the calculation indifferent to the domain size. We analyze how the image segmentation, realized to obtain the geometry from the scanned data, can also affect the numerical estimation of porous media properties.

In this paper we investigate a dry carbonate specimen (Hauptmuschelkalk) that originate from a core drilled in northern Switzerland. The corresponding CT-image raw-data is taken from [48]. The voxel size is $0.38\,\mu m^3$. Experimental results indicate a porosity of 4.2%, a permeability of $4 \times 10^{-4} mD$ and a p-wave velocity from 5100 m/s (0 MPa confining pressure) to 6100 m/s (150 MPa confining pressure).

We conduct segmentations of the Hauptmuschelkalk CT-scan with varying parameters and calculate the corresponding material geometries and the porosity of the medium. We then simulate elastic wave propagation in the porous medium to estimate segmentation-related effective elastic properties. In addition we determine the intrinsic permeability of the porous medium. Finally we discuss our results with respect to laboratory results.

2. Image segmentation

The first step in the Hauptmuschelkalk image segmentation process is to apply a 3D non-local mean filter in 3D to the Hauptmuschelkalk sample. This 3D filter takes significantly more resources than the 2D filter, but allows the avoidance

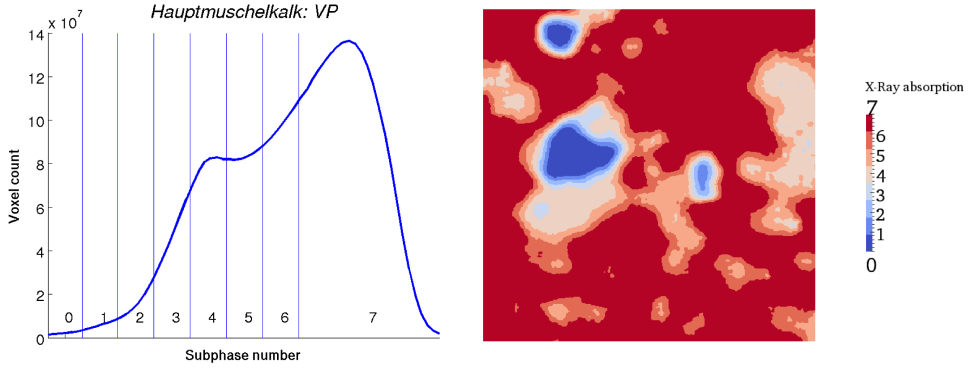

FIGURE 4.1. Image segmentation. Left: X-Ray absorption vs. voxel count. Right: Slice of mapped X-ray absorption index.

of spurious artifacts. The image segmentation is accomplished with the software Avizo.

Based on the curve shown in Figure 1 we define 8 segments enumerated from 0 to 7 (0 = porous phase, 7 = solid phase). From 6 to 1 the certainty of representing the solid phase decreases.

Figure 4.1 shows a slice normal to the Z axis of a sample subdomain. The X-ray absorption value is mapped into the voxels. We define up to 7 geometries, defining pore space and solid according to the X-ray absorption index. As an example, for the geometry named '7-6' the voxels with index absorption equal to 7 and 6 are considered solid, and voxels with a different index are considered pore space.

3. Subsample selection

The size of the original sample of Hauptmuschelkalk is $1600 \times 1600 \times 1600$ voxels. For simulation purposes we divide the sample in 64 subdomains of $400 \times 400 \times 400$ voxels. We then select statistically the most representative subdomain for our simulations. We estimate the porosity for the 7 geometries of the subdomain. The porosities of every sample are normalized, and the variance calculated for each subdomain. We finally chose the subdomain with the lowest variance.

4. Elastic Moduli

To obtain effective p-wave velocities of the digitized rock sample we use a technique described in detail in [49]. The basic idea of this approach is to study speeds of elastic waves through heterogeneous materials in the long wavelength limit (pore size $\ll$ wavelength). The RSG FD algorithm ([22]) is used for dynamic wave propagation measurements. A recent benchmark paper of this and related methods is given in [40].

Sample name	Porosity	P-wave velocity [m/s]	Permeability[m^2]
7	37.59	4146	-
7-6	25.74	4716	2.447×10^{-10}
7-6-5	14.70	5270	1.4393×10^{-10}
7-6-5-4	2.76	6040	-
7-6-5-4-3	1.64	6142	-
7-6-5-4-3-2	1.20	6184	-
7-6-5-4-3-2-1	0.84	6195	-

TABLE 4.1. Hauptmuschelkalk sample parameters

5. Permeability

We estimate the intrinsic permeability for the selected sample of Hauptmuschelkalk, from the pressure and velocity field calculated with a Stokes flow solver. The Hauptmuschelkalk presents disconnected pores that do not affect the permeability values, but can influence the performance of the solver. We realize a geometrical pre-processing of the sample, where no-connected pores are eliminated. From the velocity field we calculate volume average of the velocity u_m. μ is the viscosity of the fluid, and the pressure difference Δp is described by boundary conditions. From the previous values we calculate the permeability $k^s = (\mu u_m)/\Delta p$.

6. Results

Table 4.1 shows a summary of the numeric results. For each set of marked voxels, we calculate porosity, p-wave velocity and permeability. The permeability is not calculated in the cases where non- connectivity between input and outlet planes exists.

In Figure 4.2 (right) we compare our numerical estimates of p-wave velocities (green and blue dots) with the velocity trend based on the upper Hashin-Shtrikman bound (solid green line). We apply two, in principal, different ways of assigning elastic values to the segmented phases illustrated in Figure 4.1. For the green dots connected with a dashed line we strictly use only two different materials: solid and vacuum. The porosity is always increased by assigning one complete intermediate phase more (6 to 1) to the pore space. For the blue dots connected with the dashed line we vary the porosity by assigning to phase 1-6 effective elastic properties based on the trend given by the simulations using two single phases only.

There are two important observations. The two-phase trend (dashed line with green dots) seems to be an upper bound for the p-wave velocity. This data-driven upper bound is much stricter as the bound given by Hashin-Shtrikman. The trend given by the blue dots is not a strict lower bound; the shape will depend a lot on the applied method to determine effective elastic properties for areas which are below the resolution limit of the used CT-technique.

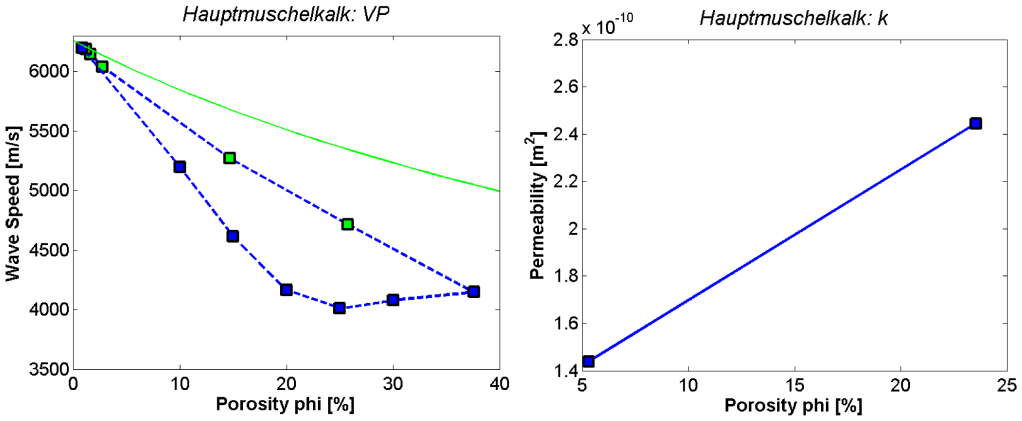

FIGURE 4.2. Left: Effective p-wave velocities for the considered Hauptmuschelkalk specimen. Green dots connected with a dashed line: Results for simulations using two different phases: solid and pores. Blue dots connected with a dashed line: Results for simulations using three different phases: solid, pores, and an intermediate phase. The porosity is varied by assigning effective elastic properties to the intermediate phase. Right: Hauptmuschelkalk Permeability. Please note: In the permeability plot we display our results with respect to the connected porosity. The total porosity is higher (see Table 4.1).

Figure 4.2 (left) shows the permeability values calculated. The porosity values change from the values exposed in Table 4.1 because we have eliminated the no-connected pores. This pores do not affect the permeability values, given that no fluid reaches them.

7. Conclusions and Discussion

With modern imaging techniques, it remains difficult to resolve microstructures (on submicrometer scale) and image a representative volume at the same time, which is essential to understand the elastic properties of rocks. To overcome this problem, we suggest a careful calibration of DRP estimates with laboratory data. For carbonate samples it is difficult to estimate the porosity from raw-CT data. Therefore we use our presented numerical results in an inverse way. We use the porosity determination from the laboratory (4.2%) and go back to Table 1 and Figure 2. With the given porosity we can estimate a permeability of 0 mD because no-connected pore systems can be resolved at this porosity. For the p-wave velocity we obtain for a porosity of 4.2% a velocity around 5800 m/s. Both results are in a reasonable agreement with the laboratory data; however, for such a low permeable rock the resolution of the CT is not sufficient for an exact estimate. Nevertheless, the suggested workflow in this paper can be applied in general for numerical estimates of mechanical and transport properties of Carbonates.

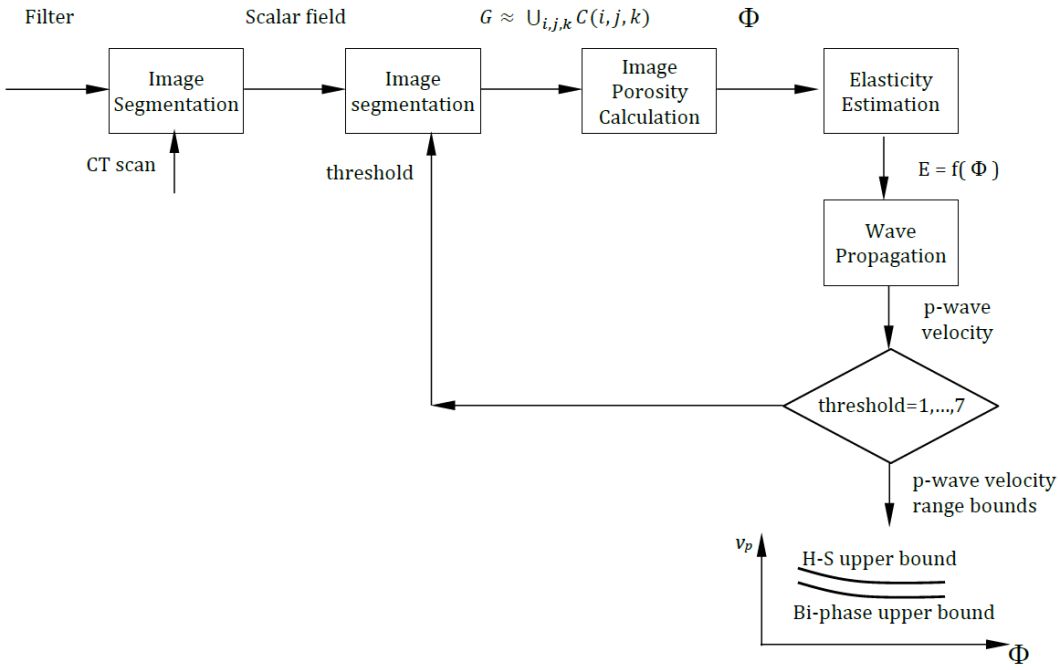

FIGURE 4.3. Workflow diagram to calculate effective properties of Carbonates.

CHAPTER 5

Determining the limits of geometrical tortuosity from seepage flow calculations in porous media.

D. Uribe[2], M. Osorno[1], R. Sivanesapillai[2,3], H. Steeb[2], and O. Ruiz[1].
[1] CAD/CAM/CAE Laboratory, Universidad EAFIT, Medellin, Colombia.
[2] Institute of Mechanics, Ruhr-University Bochum, Germany.
[3] Interdisciplinary Centre for Advanced Materials Simulation (ICAMS), Ruhr-University Bochum

The hydraulic tortuosity of porous media estimated from the streamlines of a flow through the material presents a dependence on the flow Reynolds number, with a upper limit at low Re and a lower limit at high Re (resembling a Sigmoid function). This paper proposes a geometrical method to estimate the lower limit of tortuosity from streamlines calculated at low Reynolds, avoiding the difficulties that present high Re simulations.
This research was made on collaboration between the Laboratory of CAD CAM CAE at Universidad EAFIT and the Institute of Mechanics at Ruhr-University Bochum. This paper was presented at the 85th Annual Meeting of the International Association of Applied Mathematics and Mechanics (GAMM) in Erlangen, Germany, March 10-14, 2014. This paper will be published on the Journal Proceedings of Applied Mathematics and Mechanics (PAMM). ISSN 1617-7061. WILEY-VCH Verlag. December, 2014.

Abstract. Recent discoveries have found a distinct correlation of effective properties of porous media to sigmoid functions, where one axis is the Reynolds number Re and the other is the effective property dependent of Re, $\Theta_i = S_i(Re)$. One of these properties is tortuosity. At very low Re (seepage flow), there is a characteristic value of the tortuosity, and it is the upper horizontal asymptote of the sigmoid function. With higher values of Re (transient flow) the tortuosity value decreases, until a lower asymptote is reached (turbulent flow).

Estimations of this parameter have been limited to the low Reynolds regime in the study of porous media. The current state of the art presents different numerical measurements of tortuosity, such as skeletization, centroid binding, and arc length of streamlines. These are solutions for the low Re regime. So far, for high Re, only the arc length of stream lines has been used to calculate the tortuosity value. This approach involves the simulation of fluid flow in large domains and high Re, which requires numerous resources, and often presents convergence problems. In response to this, we propose a geometrical method to estimate the limit of tortuosity of porous media at $Re \to \infty$, from the streamlines calculated at low Re limit. We test our method calculating the tortuosity limits in a fibrous porous media, and comparing the estimated values with benchmark results. Ongoing work includes the geometric estimation of different intrinsic properties of porous media.

1. Introduction

Hydraulic tortuosity presents different definitions ([38]). In our case we define tortuosity as the ratio streamline arclength vs. length of the Representative Volume Element (RVE) in the flow direction. Simulations on recent investigations ([50]) show that the tortuosity presents an upper plateau for low Re and a lower plateau for high Re, with a monotonically decreasing connection at middle Re (resembling a Sigmoid function).

At low Reynolds regimes ($Re < 1.0$), tortuosity is normally estimated from CFD simulations or geometrical (e.g. centroid binding, medial axis) methods. High Re regimes ($Re > 10^3$) convergence presents difficulties for CFD, and accordingly, there are no reports of geometric methods to calculate tortuosity at these limits. We remark that flows with high inertial forces (at high Re) present streamlines with lower curvatures. Therefore, we implement a method to eliminate high frequencies (i.e. lower the curvatures) from the low Re streamlines. From the filtered streamlines, it is possible to estimate the tortuosity, without resorting to high Re CFD calculations.

2. Methodology

We propose two geometrical methods to estimate the low limit of tortuosity (high Re) of a porous media, which solid phase is conformed by convex subdomains (Fig. 5.1), from the streamlines (with coordinates (x_0^i, y_0^i), $0 \leq i \leq n$) calculated of a 2D velocity field describing a low Re flow in Y-axis direction.

2.1. Shooting method. We estimate new streamlines with coordinates (x_1^i, y_1^i) from the low Re streamlines: (1) Define seed point $(x_1^0, y_1^0) = (x_0^0, y_0^0)$, (2) define next point of new streamline $x_1^i = x_1^{i-1}$ and $y_1^i = y_0^i$, (3) repeat step (2) until $(x_1^i, y_1^i) \in \Omega_s$ or $i = n$, (4) If $(x_1^i, y_1^i) \in \Omega_s$, define $x_1^i = x_1^i + \text{sign}(x_0^i - x_1^i)$, (5) Repeat step (4) until $(x_1^i, y_1^i) \notin \Omega_s$ and (6) Repeat steps (2)-(5) until $i = n$

2.2. Stretching method. We apply a filter to the low Re streamlines with coordinates (x_0^i, y_0^i) to obtain the new streamlines (x_k^i, y_k^i) with the lower curvature possible without overlapping the obstacles: (1) $x_k^i = x_{k-1}^i + w(\frac{x_k^{i-1}+x_k^{i+1}}{2})$, $y_k^i = y_0^i$, with $i = 2...n-1$. If $(x_k^i, y_k^i) \in \Omega_s$, then $(x_k^i, y_k^i) = (x_k^i - 1, y_k^i - 1)$. (2) Repeat step (1) until $k = m$ where $\sum_{i=1}^{n-1} |x_m^i - x_{m-1}^i| < \varepsilon$

3. Results

Fig. 5.1 shows a subdomain of the fibrous porous media analysed, the low Re streamlines (blue lines) calculated in ([50]), and the new streamlines (red lines) after applying the shooting method (Fig. 1(a)) and the stretching method (Fig. 1(b)). The low limit of tortuosity is calculated from the new streamlines.

The data obtained from measuring the tortuosity of each streamline describes a Gaussian distribution (Fig. 5.2). The blue line describes the Gaussian distribution of the tortuosity upper limit and the red line of the lower limit. The dashed lines indicates the reference values of low Re tortuosity (blue) and high Re tortuosity (red) ([50]).

Tab. 5.1 presents a comparison between the estimated tortuosity and the reference values. Tortuosity at low Re varies from the reference value due to the different methods for tortuosity measurement. The shooting method presents an error of 1.3%, and the stretching method an error of 2.7%.

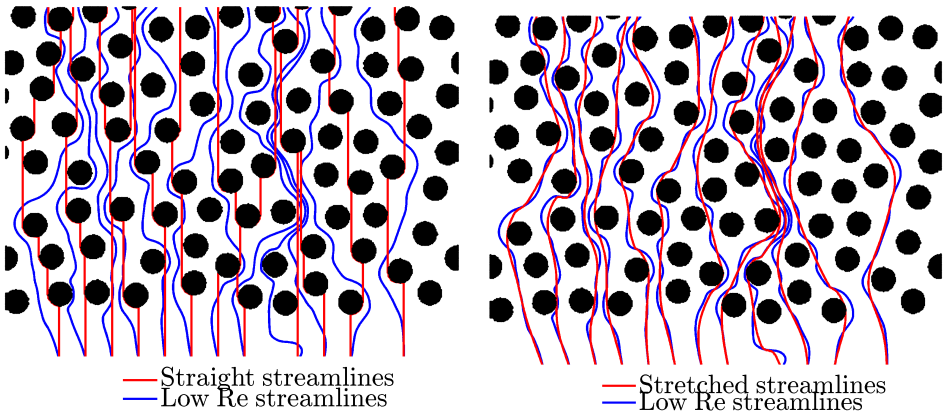

(a) Shooting method (b) Stretching method

FIGURE 5.1. Modified streamlines

4. Conclusions and Future Work

We have developed two geometrical methods to estimate the tortuosity lower limit (high Re). The proposed methods present a low error with respect to the reference values and are orders of magnitude computational cheaper than CFDs

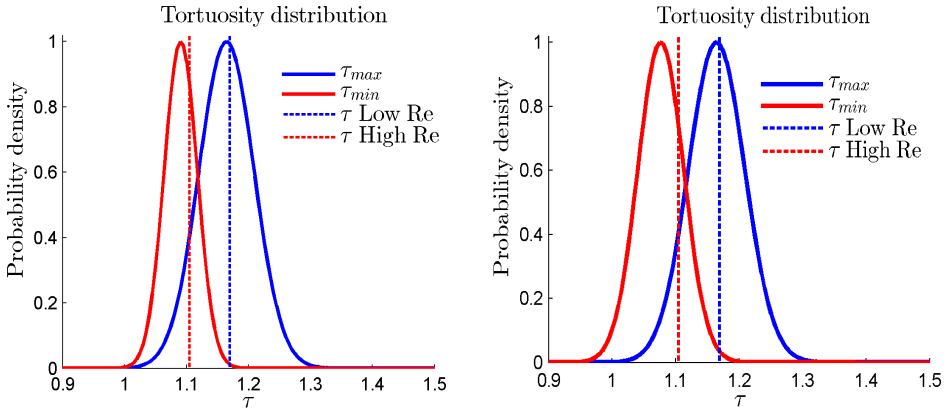

(a) Shooting method (b) Stretching method

FIGURE 5.2. Tortuosity distribution

	Reference ([50])	Shooting method	Stretching method
τ low Re	1.1696	1.165	1.165
τ high Re	1.1051	1.090	1.075

TABLE 5.1. Results of tortuosity estimation.

simulations.

Future work includes the mapping of geometrical parameters of the streamlines into Re number at the transition zone.

CHAPTER 6

Response to Reviewers Observations

1. Geometrical and numerical modeling for porous media wave propagation

Tables 6.1 and 6.2 show the response to the observations that reviewers made on the article "Geometrical and numerical modeling for porous media wave propagation" presented in chapter 1.

Observation	Response
More accurate description of the adopted foam and software must be included.	We complied with this request by adding in section 3 this text: In the present case the analyzed porous material is 10 ppi AlSi7Mg foam (Fig. 1.1) by m.pore GmbH. Tab. 1.1 shows the modelling parameters of the aluminum foam.
The style of the rest of the paper seems not to be consistent with the declaration of the type of the paper (an industrial and application paper).	We have addressed the observation of the Reviewer. We have explicated the industrial application of our manuscript by intervening the Sections 1 and 3.
In the figures units must be specified.	We have added the units to the figures 3(a), 7(b) and 9(b).

TABLE 6.1. Response to reviewers observations to article "Geometrical and numerical modeling for porous media wave propagation". Part I

Observation	Response
The theoretical bases are introduced by a huge formalism (more appropriate for a research paper) that unfortunately does not help to explain its practical use and limits according to the specific application	We have indeed the intention of writing an applied research article. To make it accessible, we have added an explanation about the practical use and limitations of our approach in sections 1 and 3. "In this article we implement and apply several geometrical processing methods to represent solids from industrial micro CT scans of porous materials. The different representations of the material (voxels, slices contours, triangular meshes and parametric surfaces), allows simulations in the middle steps of the process. We can also manage the porous media information with a lower memory usage. Finally with the parametric surfaces of the material, is possible the use of robust commercial CAE software that can not manage voxel-based information.
According to my experience the paper covers a difficult topic that involves many research areas (reverse engineering of cellular structure from 2D scan, FEM modeling and simulation). The state of the art clearly explains the reverse engineering topics. It is less complete for the simulation part.	We have addressed the observation of the Reviewer by focusing on the topic of the paper, which is a complex geometrical manipulation of CT-Data into a smooth-surface representation. In addition, the State of the Art in simulation was complemented with the articles [26], [22], [23], [25] and [24].
Many details of the works that concern the general applicability of the results are not clear to me (e.g. what is the height of the simulated foam sample?).	The reviewer is right. Because the numerical simulations are computationally prohibitive, existing literature addresses very limited scopes. Our research seeks to contribute in easing this limitation. We have addressed the observation of the Reviewer by complementing the Results section (Sec. 4) with details about the simulation. Fig. 7(a) shows the simulation setup and the axis on Fig. 7(b) indicates the scale of the simulation.
No information is given in term of entry data hypothesis, algorithm complexity, treatment time or precision performance for the proposed approach	We have addressed the Reviewer's observation by citing the papers ([26], [22], [23], [25] , [24]) with the simulation State of the Art, where this point is addressed.

TABLE 6.2. Response to reviewers observations to article "Geometrical and numerical modeling for porous media wave propagation". Part II

2. Estimation of large domain Al foam permeability by Finite Difference methods

Table 6.3 presents the response to the observations of the reviewers to the paper "Estimation of large domain Al foam permeability by Finite Difference methods" presented in chapter 2.

Observation	Response
In the figures units must be specified	Units were added to the figure 2.1.
Write the method in form of step sequence.	The following text was added: " (I) Discretization of equations (3) and (5) on a staggered grid by using a 2nd order FD method with periodic boundary conditions for velocity in the inlet and outlet of the channel (Fig. 2.1). (II) Solution of the resulting equation system with the iterative Gauss-Seidel scheme. The Gauss-Seidel method does not require to store a coefficient matrix. (III) Calculation of the volume averaged velocity u_m from the velocity field computed in step 2. (IV) Estimation of the medium permeability with Darcy's law (Eq. 14)"
Use active voice as possible.	Some sentences were modified to use active voice, e.g. : "Figure 2(b) shows the velocity in Z direction on plane YZ at x= 12mm. "
Modify permeability and porosity nomenclature.	The permeability nomenclature K_D was replaced by k_D^s. The porosity nomenclature ϵ was replaced by ϕ.
Setup the velocity in figure 2.1 in either vertical positive direction of towards the reader.	The velocity direction in figure 2.1 was modified to vertical positive direction.
Explain the use of the domain in figure 2(a), if there are much more realistic geometries.	The following text was added: "The method was validated with a regular packed sphere case in 3D (Fig. 2(a)) whose permeability can be calculated with the Carman-Kozeny model proposed in [36]."

TABLE 6.3. Response to reviewers observations to article "Estimation of large domain Al foam permeability by Finite Difference methods". Part I

Observation	Response
Change 'Equation' for 'Eq.'. Make it consistent all over the paper.	The references to equations were replaced by 'Eq.', e.g., "Estimation of the medium permeability with Darcy's law (Eq. 14)"
Add dimensions in 'mm' to the figure 2.1 caption.	The text "(24mm $\times$ 24mm $\times$ 24mm)" was added to the caption of figure 2.1.

TABLE 6.4. Response to reviewers observations to article "Estimation of large domain Al foam permeability by Finite Difference methods". Part II.

3. Finite difference estimation of permeability in large domains in a wide porosity range

Table 6.5 shows the response to the observations of the reviewers to the paper "Finite difference estimation of permeability in large domains in a wide porosity range" presented in chapter 3.

Observation	Response
Add figure with task-block describing the proposed workflow.	The figure 3.1 was added to describe the workflow.
Illustrate completly the geometric scenario of the physical problem	The figure 3.3 was added describing the domains and the problem set-up.
Illustrate the parallelization procedure.	The figure 3.5 was added to describe the domain division in the parallel solver.
Include results for different discretizations of capillary tube in figure 3.8 to compare the method performance with different grids.	The results obtained with coarser grids of the capillary tube were added to the figure 3.8.
Include more information about the proposed parallelization	The following text was added about the parallelization: "Given the advantage of using distributed memory in our problem, we parallelized the computation using MPICH2 (Message Passing Interface based on Chameleon portability system). The domain was divided between the processes in a straightforward way. We split the domain with a family of equidistant planes, normal to the Z axis, according to the number of cores used. Fig. 3.5 shows an example of the domain division proposed for the code parallelization. In parallel computation the communication among processes represents a resources-consuming task. We minimize this communication expense by having each process to pass to the neighboring one only a slice of the domain (gray voxels in Fig. 3.5). The communication operations were organized in a ring network ([45]), where we can find a communication link between the first and last process."

TABLE 6.5. Response to reviewers observations to article "Finite difference estimation of permeability in large domains in a wide porosity range"

4. Numerical estimation of carbonate properties using a digital rock physics workflow

Table 6.6 shows the response to the observations of the reviewers to the paper "Numerical estimation of carbonate properties using a digital rock physics workflow" presented in chapter 4.

Observation	Response
Add figure with Task-Block describing the workflow.	The figure 4.3 was added to explain the proposed workflow to calculate effective properties of Carbonates
Express clearly the characteristics of the analysed sample.	The following text was added to describe the material sample: "In this paper we investigate a dry carbonate specimen (Hauptmuschelkalk) that originate from a core drilled in northern Switzerland. The corresponding CT-image raw-data is taken from [48]. The voxel size is $0.38\,\mu m^3$. Experimental results indicate a porosity of 4.2%, a permeability of $4 \times 10^{-4} mD$ and a p-wave velocity from 5100 m/s (0 MPa confining pressure) to 6100 m/s (150 MPa confining pressure)."

TABLE 6.6. Response to reviewers observations to article "Numerical estimation of carbonate properties using a digital rock physics workflow"

5. Determining the limits of geometrical tortuosity from seepage flow calculation in porous media

Table 6.7 shows the response to the observations of the reviewers to the paper "Determining the limits of geometrical tortuosity from seepage flow calculation in porous media" presented in chapter 5.

Observation	Response
Express clearly the necessary initial conditions for the proposed methods.	The following text was added to explain the initial conditions of the problem: "...which solid phase is conformed by convex subdomains (Fig. 5.1), from the streamlines (with coordinates (x_0^i, y_0^i), $0 \leq i \leq n$) calculated of a 2D velocity field describing a low Re flow in Y-axis direction."
The proposed methods must be expressed in a formal discourse and must be un-ambiguous.	The text in the methodology section was modified: "We estimate new streamlines with coordinates (x_1^i, y_1^i) from the low Re streamlines: (1) Define seed point $(x_1^0, y_1^0) = (x_0^0, y_0^0)$, (2) define next point of new streamline $x_1^i = x_1^{i-1}$ and $y_1^i = y_0^i$, (3) repeat step (2) until $(x_1^i, y_1^i) \in \Omega_s$ or $i = n$, (4) If $(x_1^i, y_1^i) \in \Omega_s$, define $x_1^i = x_1^i + \text{sign}(x_0^i - x_1^i)$, (5) Repeat step (4) until $(x_1^i, y_1^i) \notin \Omega_s$ and (6) Repeat steps (2)-(5) until $i = n$"
Specify how the results in the figure 5.2 were calculated.	The following text was added to explain the figure: "The data obtained from measuring the tortuosity of each streamline describes a Gaussian distribution (Fig. 5.2). The blue line describes the Gaussian distribution of the tortuosity upper limit and the red line of the lower limit. The dashed lines indicates the reference values of low Re tortuosity (blue) and high Re tortuosity (red) ([50])."

TABLE 6.7. Response to reviewers observations to article "Determining the limits of geometrical tortuosity from seepage flow calculation in porous media"

Conclusions

This work presents different methods to estimate effective properties of porous materials, such as permeability, porosity, tortuosity and compressional and shear moduli. The numerical methodologies are also exposed here.

A workflow was proposed to obtain parametric surfaces (compatible with CAE commercial packages) from micro CT-data, including the intermediate steps of voxels, plane-wise contours and triangular mesh. The geometrical results were validated with a simulation of wave propagation and calculation of geometrical properties of the medium. The proposed workflow produces a geometrical representation that facilitates the analysis of any porous media structure. The resulting geometrical representation is generated in widely used computational formats, which allow the collaboration between different research groups.

A parallel Finite Difference solver was implemented to simulate a Stokes flow through domains large enough to be representative of a porous material's microstructure (geometrically represented with voxels), which was not possible with a desktop computer using commercial packages due to computational memory requirements. From the pressure and velocity fields calculated, it was possible to estimate the material permeability using Darcy's Law. The method was applied to porous materials with porosities in the range of $[0.146 - 0.934]$. The results were validated with benchmark references.

An image segmentation procedure is proposed to overcome the difficulties involved in resolving a carbonate microstructure. A workflow was implemented for estimating the permeability, porosity and the effective wave velocities in carbonates from a CT scanned sample. It was possible to find an adjusted Hashin-Shtrikman upper bound.

A geometrical method was proposed to estimate the tortuosity limits for a fibrous porous medium from the Stokes flow streamlines. With the proposed method it is possible to calculate the low limit of tortuosity without simulating the flow at high Reynolds.

Bibliography

[1] S. Gasser, F. Paun, and Y. Brechet. Absorptive properties of rigid porous media: Application to face centered cubic sphere packing. *The Journal of the Acoustical Society of America*, 117:2090, 2005.

[2] A. S. Phani, J. Woodhouse, and NA Fleck. Wave propagation in two-dimensional periodic lattices. *The Journal of the Acoustical Society of America*, 119:1995, 2006.

[3] O. Wirjadi. *Survey of 3d image segmentation methods*. ITWM, 2007.

[4] W. Oh and B Lindquist. Image thresholding by indicator kriging. *Pattern Analysis and Machine Intelligence, IEEE Transactions on*, 21(7):590–602, 1999.

[5] M. Sezgin and B. Sankur. Survey over image thresholding techniques and quantitative performance evaluation. *Journal of Electronic Imaging*, 13(1):146–165, 2004.

[6] R. Adams and L. Bischof. Seeded region growing. *Pattern Analysis and Machine Intelligence, IEEE Transactions on*, 16(6):641–647, 1994.

[7] V. Caselles, R. Kimmel, G. Sapiro, and C. Sbert. Minimal surfaces based object segmentation. *Pattern Analysis and Machine Intelligence, IEEE Transactions on*, 19(4):394–398, 1997.

[8] P. Iassonov and M. Tuller. Application of segmentation for correction of intensity bias in x-ray computed tomography images. *Vadose Zone Journal*, 9(1):187–191, 2010.

[9] W. E. Lorensen and H. E. Cline. Marching cubes: A high resolution 3d surface construction algorithm. *SIGGRAPH Comput. Graph.*, 21(4):163–169, August 1987.

[10] N. Amenta, S. Choi, and R. K. Kolluri. The power crust. In *Proceedings of the sixth ACM symposium on Solid modeling and applications*, SMA '01, pages 249–266, New York, NY, USA, 2001. ACM.

[11] O. Ruiz, C. Cadavid, M. Granados, S. Pena, and E. Vásquez. 2d shape similarity as a complement for voronoi-delone methods in shape reconstruction. *Computers & Graphics*, 29(1):81–94, 2005.

[12] M. Kazhdan, M. Bolitho, and H. Hoppe. Poisson surface reconstruction. In *Symposium on Geometry Processing*, pages 61–70, 2006.

[13] O. Ruiz, C. Vanegas, and C. Cadavid. Principal component and voronoi skeleton alternatives for curve reconstruction from noisy point sets. *Journal of Engineering Design*, 18(5):437–457, 2007.

[14] M. Desbrun, M. Meyer, and P. Alliez. Intrinsic parameterizations of surface meshes. In *Computer Graphics Forum*, volume 21, pages 209–218. Wiley Online Library, 2002.

[15] B. Jüttler and A. Felis. Least-squares fitting of algebraic spline surfaces. *Advances in Computational Mathematics*, 17(1-2):135–152, 2002.

[16] S. Petitjean. A survey of methods for recovering quadrics in triangle meshes. *ACM Computing Surveys (CSUR)*, 34(2):211–262, 2002.

[17] J. Boissonnat and B. Geiger. Three-dimensional reconstruction of complex shapes based on the delaunay triangulation. In *IS&T/SPIE's Symposium on Electronic Imaging: Science and Technology*, pages 964–975. International Society for Optics and Photonics, 1993.

[18] M. Morse. *The Calculus of Variations in the Large*. American Mathematical Society: Colloquium publications. American Mathematical Society, 1932.

[19] O. Ruiz, S. Arroyave, D. Acosta, C. Cadavid, and J. Londono. Manifold learning for optimized fitting of freeform surfaces. In *Symposium on Geometry Processing 2013*, 2013. Submitted.

[20] P. Kurzeja and H. Steeb. About the transition frequency in biot's theory. *The Journal of the Acoustical Society of America*, 131(6):EL454–EL460, 2012.

[21] M. A. Biot. Theory of propagation of elastic waves in a fluid-saturated porous solid. II. High-frequency range. *Journal of the Acoustical Society of America*, 29:168–191, 1956.

[22] E. H. Saenger, N. Gold, and S. A. Shapiro. Modeling the propagation of elastic waves using a modified finite-difference grid. *Wave Motion*, 31(1):77 – 92, 2000.

[23] E. H. Saenger and S. A. Shapiro. Effective velocities in fractured media: A numerical study using the rotated staggered finite-difference grid. *Geophysical Prospecting*, 50:183–194, 2002.

[24] J. Virieux. Velocity-stress finite-difference method. *Geophysics*, 51:889–901, 1986.

[25] E. H. Saenger, S. A. Shapiro, and Y. Keehm. Seismic effects of viscous biot-coupling: Finite difference simulations on micro-scale. *Geophysical Research Letters*, 32(14):n/a–n/a, 2005.

[26] E. H. Saenger. Numerical methods to determine effective elastic properties. *International Journal of Engineering Science*, 46(6):598 – 605, 2008. Special Issue: Micromechanics of Materials.

[27] H. Steeb. Ultrasound propagation in cancellous bone. *Archive of Applied Mechanics*, 80:489–502, 2010.

[28] I. Gueven, P. Kurzeja, S. Luding, and H. Steeb. Experimental evaluation of phase velocities and tortuosity in fluid saturated highly porous media. *PAMM*, 12(1):401–402, 2012.

[29] I. Gueven, S. Luding, and H. Steeb. Hydraulic and acoustic investigation of sintered glass beads. *AIP Conference Proceedings*, 1542(1):581–584, 2013.

[30] J. G. Fourie and J. P. Du Plessis. Pressure drop modelling in cellular metallic foams. *Chemical Engineering Science*, 57(14):2781–2789, 2002.

[31] L.P. Lefebvre, J. Banhart, D. Dunand, et al. Porous metals and metallic foams: current status and recent developments. *Advanced Engineering Materials*, 10(9):775–787, 2008.

[32] O. Gerbaux, F. Buyens, VV Mourzenko, A. Memponteil, A. Vabre, J.F. Thovert, and PM Adler. Transport properties of real metallic foams. *Journal of colloid and interface science*, 342(1):155–165, 2010.

[33] W. Xu, H. Zhang, Z. Yang, and J. Zhang. Numerical investigation on the flow characteristics and permeability of three-dimensional reticulated foam materials. *Chemical Engineering Journal*, 140(1):562–569, 2008.

[34] J. Petrasch, F. Meier, H. Friess, and A. Steinfeld. Tomography based determination of permeability, dupuit-forchheimer coefficient, and interfacial heat transfer coefficient in reticulate porous ceramics. *International Journal of Heat and Fluid Flow*, 29(1):315–326, 2008.

[35] A. Nabovati, E.W. Llewellin, and A. Sousa. A general model for the permeability of fibrous porous media based on fluid flow simulations using the lattice boltzmann method. *Composites Part A: Applied Science and Manufacturing*, 40(6):860–869, 2009.

[36] P.C. Carman. *Flow of gases through porous media*. Academic Press, 1956.

[37] H. Rumpf and A. Gupte. Einflüsse der porosität und korngrößenverteilung im widerstandsgesetz der porenströmung. *Chemie Ingenieur Technik*, 43(6):367–375, 2004.

[38] S.C. Cowin and L. Cardoso. Difficulties arising from different definitions of tortuosity for wave propagation in saturated poroelastic media models. *ZAMM - Journal of Applied Mathematics and Mechanics*, 11:1–11, 2013.

[39] C. Manwart, U. Aaltosalmi, A. Koponen, R. Hilfer, and J. Timonen. Lattice-boltzmann and finite-difference simulations for the permeability for three-dimensional porous media. *Physical Review E*, 66(1):016702, 2002.

[40] H. Andrä, N. Combaret, J. Dvorkin, E. Glatt, J. Han, M. Kabel, Y. Keehm, F. Krzikalla, M. Lee, C. Madonna, et al. Digital rock physics benchmarkspart ii: Computing effective properties. *Computers & Geosciences*, 50:33–43, 2013.

[41] K. Boomsma, D. Poulikakos, and Y. Ventikos. Simulations of flow through open cell metal foams using an idealized periodic cell structure. *International Journal of Heat and Fluid Flow*, 24(6):825–834, 2003.

[42] H. Andrä, N. Combaret, J. Dvorkin, E. Glatt, J. Han, M. Kabel, Y. Keehm, F. Krzikalla, M. Lee, C. Madonna, et al. Digital rock physics benchmarks–part i: Imaging and segmentation. *Computers & Geosciences*, 2012.

[43] S. Nagarajan, S.K. Lele, and J.H. Ferziger. A robust high-order compact method for large eddy simulation. *Journal of Computational Physics*, 191(2):392–419, 2003.

[44] D. Young. Iterative methods for solving partial difference equations of elliptic type. *Transactions of the American Mathematical Society*, 76(1):92–111, 1954.

[45] T. Rauber and G. Rünger. *Parallel programming: For multicore and cluster systems*. Springer, 2010.

[46] H. Darcy. *Les fontaines publiques de la ville de Dijon*. V. Dalmont, 1856.

[47] P. Carman. Permeability of saturated sands, soils and clays. *Journal of Agricultural Science*, 29:262–273, 1939.

[48] C. Madonna, B. Quintal, M. Frehner, B.S.G. Almqvist, Pistone M. Tisato, N., F. Marone, and E. H. Saenger. Synchrotron-based x-ray tomographic microscopy for rock microstructure investigations. *Geophysics*, 78:D53–D64, 2013.

[49] E. H. Saenger, O. Krüger, and S. Shapiro. Effective elastic properties of randomly fractured soils: 3d numerical experiments. *Geophysical Prospecting*, 52(3):183–195, 2004.

[50] R. Sivanesapillai, H. Steeb, and A. Hartmaier. Transition of effective hydraulic properties from low to high reynolds number flow in porous media, 2014.